Manuscript Details

Manuscript number	CBAC_2020_1149
Title	Interaction of small molecules with the SARS-CoV-2 main protease in silico and in vitro validation of potential lead compounds using an enzyme-linked immunosorbent assay
Article type	Research Paper

Abstract

Caused by the severe acute respiratory syndrome coronavirus 2 (SARS-CoV-2), the COVID-19 pandemic is ongoing, with no proven safe and effective vaccine to date. Further, effective therapeutic agents for COVID-19 are limited, and as a result, the identification of potential small molecule antiviral drugs is of particular importance. A critical antiviral target is the SARS-CoV-2 main protease (Mpro), and our aim was to identify lead compounds with potential inhibitory effects. We performed an initial molecular docking screen of 300 small molecules, which included phenolic compounds and fatty acids from our OliveNetTM library (224), and an additional group of curated pharmacological and dietary compounds. The prototypical □-ketoamide 13b inhibitor was used as a control to guide selection of the top 30 compounds with respect to binding affinity to the Mpro active site. Further studies and analyses including blind docking were performed to identify hypericin, cyanidin-3-O-glucoside and SRT2104 as potential leads. Molecular dynamics simulations demonstrated that hypericin (ΔG = -18.6 and -19.3 kcal/mol), cyanidin-3-O-glucoside (ΔG = -50.8 and -42.1 kcal/mol), and SRT2104 (ΔG = -8.7 and -20.6 kcal/mol), formed stable interactions with the Mpro active site. An enzyme-linked immunosorbent assay indicated that, albeit, not as potent as the covalent positive control (GC376), our leads inhibited the Mpro with activity in the micromolar range, and an order of effectiveness of hypericin and cyanidin-3-O-glucoside > SRT2104 > SRT1720. Overall, our findings add to the mechanisms highlighted in previous studies with hypericin and cyanidin-3-O-glucoside in various experimental models, some of which include antiviral effects.

Keywords	COVID-19; SARS-CoV-2 main protease; hypericin; cyanidin-3-O-glucoside; molecular docking; molecular dynamics simulations

Corresponding Author	Tom Karagiannis
Corresponding Author's Institution	Monash University
Order of Authors	Eleni Pitsillou, Julia Liang, Chris Karagiannis, Katherine Ververis, Kevion Darmawan, Ken Ng, Andrew Hung, Tom Karagiannis

Highlights

- The SARS-CoV-2 M^{pro} is an important viral target for the ongoing COVID-19 pandemic
- Initial screen by docking 300 small molecules to the M^{pro} active site
- Preferential binding of 3 leads to the M^{pro} active site revealed by blind docking
- Stability of lead compounds with the M^{pro} active site confirmed by MD simulations
- Hypericin and cyanidin-3-O-glucoside inhibit M^{pro} *in vitro* in micromolar range

SARS-CoV-2 main protease with covalent α-ketoamide 13b inhibitor bound in the active site

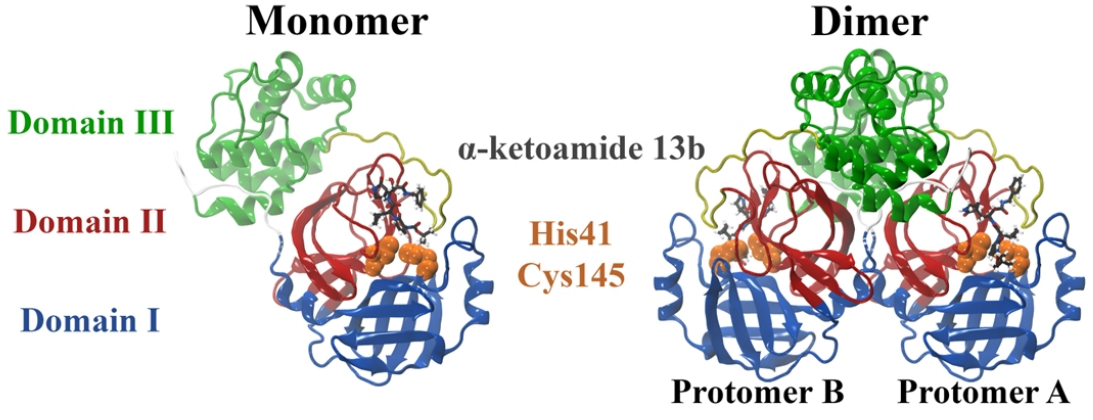

Potential lead non-convalent inhibitors of the SARS-CoV-2 main protease

Binding affinity = -10.2 kcal/mol

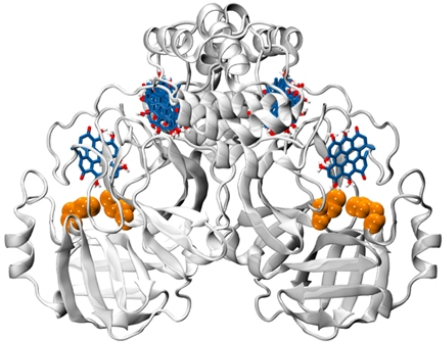

4 poses out of 20 in the active site (poses #1, 2, 3, 4)

Hypericin

Binding affinity = -9.2 kcal/mol

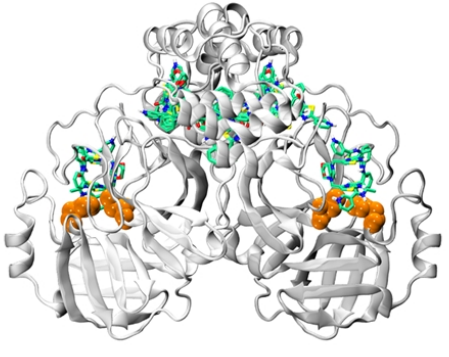

4 poses out of 20 in the active site (poses #1, 3, 10, 11)

SRT2104

Binding affinity = -8.8 kcal/mol

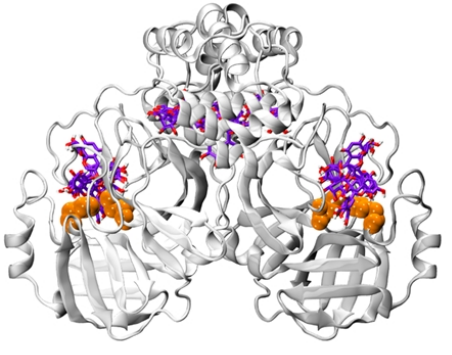

7 poses out of 20 in the active site (poses #1-4, 11, 12, 15)

Cyanidin-3-O-glucoside

Interaction of small molecules with the SARS-CoV-2 main protease *in silico* and *in vitro* validation of potential lead compounds using an enzyme-linked immunosorbent assay

Eleni Pitsillou[1,2], Julia Liang[1,2], Chris Karagiannis[2,3], Katherine Ververis[1], Kevion K Darmawan[2], Ken Ng[3], Andrew Hung[2], Tom C Karagiannis[1,4]

[1] Epigenomic Medicine, Department of Diabetes, Central Clinical School, Monash University, Melbourne, VIC 3004, Australia

[2] School of Science, College of Science, Engineering & Health, RMIT University, VIC 3001, Australia

[3] Food Chemistry, Faculty of Veterinary and Agricultural Sciences, University of Melbourne, Parkville, VIC 3052, Australia

[4] Department of Clinical Pathology, The University of Melbourne, Parkville, VIC 3052, Australia

Keywords: Coronavirus, COVID-19, SARS-CoV-2, SARS-CoV-2 main protease, hypericin, cyanidin-3-O-glucoside, molecular docking, molecular dynamics simulations

Running (short) title: SARS-CoV-2 main protease inhibitors

Author for correspondence:

Tom Karagiannis, PhD

Head Epigenomic Medicine Program

Department of Diabetes

Central Clinical School

Monash University

Melbourne, VIC 3004, Australia

Abstract

Caused by the severe acute respiratory syndrome coronavirus 2 (SARS-CoV-2), the COVID-19 pandemic is ongoing, with no proven safe and effective vaccine to date. Further, effective therapeutic agents for COVID-19 are limited, and as a result, the identification of potential small molecule antiviral drugs is of particular importance. A critical antiviral target is the SARS-CoV-2 main protease (M^{pro}), and our aim was to identify lead compounds with potential inhibitory effects. We performed an initial molecular docking screen of 300 small molecules, which included phenolic compounds and fatty acids from our OliveNet™ library (224), and an additional group of curated pharmacological and dietary compounds. The prototypical α-ketoamide 13b inhibitor was used as a control to guide selection of the top 30 compounds with respect to binding affinity to the M^{pro} active site. Further studies and analyses including blind docking were performed to identify hypericin, cyanidin-3-O-glucoside and SRT2104 as potential leads. Molecular dynamics simulations demonstrated that hypericin (ΔG = -18.6 and -19.3 kcal/mol), cyanidin-3-O-glucoside (ΔG = -50.8 and -42.1 kcal/mol), and SRT2104 (ΔG = -8.7 and -20.6 kcal/mol), formed stable interactions with the M^{pro} active site. An enzyme-linked immunosorbent assay indicated that, albeit, not as potent as the covalent positive control (GC376), our leads inhibited the M^{pro} with activity in the micromolar range, and an order of effectiveness of hypericin and cyanidin-3-O-glucoside > SRT2104 > SRT1720. Overall, our findings add to the mechanisms highlighted in previous studies with hypericin and cyanidin-3-O-glucoside in various experimental models, some of which include antiviral effects.

Introduction

On the 31st of December 2019, the health authorities in China's Hubei province were informed that there was a cluster of patients with viral pneumonia of unknown origin in the city of Wuhan (1-3). After collecting and analysing samples that were taken from the patients, the pathogen was identified as a novel coronavirus (1-3). The genomic sequence was soon made available by the Chinese Centre for Disease Control and Prevention (China CDC) and the virus was classified as severe acute respiratory syndrome coronavirus 2 (SARS-CoV-2) by the *Coronaviridae* Study Group (CSG) of the International Taxonomy Committee of Viruses (ICTV) (2-6). The infection caused by SARS-CoV-2 was officially named Coronavirus Disease 2019 (COVID-19) by the World Health Organisation (WHO) (1, 6).

Since being declared a pandemic in early March, COVID-19 has spread rapidly throughout the world and is currently ongoing (1, 7, 8). There are currently no approved human coronavirus vaccines (9, 10). The Coalition for Epidemic Preparedness Innovations (CEPI) is providing support to vaccine developers however, there are several challenges that must be overcome before candidates are tested in clinical studies and are made available for use (9). As a result, there is an urgent need to investigate, identify and repurpose small molecules with potential antiviral effects (11). A number of clinical trials have already begun to evaluate the safety and efficacy of drugs including hydroxychloroquine, chloroquine, remdesivir, lopinavir, ritonavir and azithromycin, as well as traditional Chinese medicines (TCM) (11-17).

SARS-CoV-2 is a positive-sense single-stranded RNA virus that is enveloped and belongs to the betacoronavirus genus (3, 18, 19). In a study conducted by Zhou et al., the genetic sequences of SARS-CoV-2 and SARS-CoV were found to be 79.6% identical and SARS-CoV-2 was also 96.2% identical to a bat coronavirus (BatCoV RaTG13) at the whole-genome level (20). Like SARS-CoV, which was the causative agent of the severe acute respiratory syndrome epidemic that occurred in 2002 and 2003, there is evidence to suggest that SARS-CoV-2 binds to human angiotensin-converting enzyme 2 (ACE2) receptors to gain entry into host cells (20).

The interaction is mediated by the receptor binding domain (RBD) of the spike glycoprotein on the virion surface and the peptidase domain (PD) of ACE2 (18, 21-23). In addition to the spike glycoprotein, the coronavirus main protease (M^{pro}) is an important target for antiviral therapy (24). The replicase gene of SARS-CoV-2 encodes the replicase polyproteins, pp1a and pp1ab (19, 24, 25). M^{pro} is the enzyme that is predominantly responsible for the proteolytic processing of these polyproteins into functional polypeptides (19, 24, 25). Thus, M^{pro} plays an important role in viral replication and infection (19).

There is a growing body of literature on lead compounds that could be used to target the M^{pro} enzyme of SARS-CoV-2. This includes peptidomimetics, such as α-ketoamide inhibitors (19, 22, 26). Aside from synthetic ligands, researchers are also investigating the antiviral properties of natural compounds and dietary polyphenols have been of particular interest (24, 27-30). Extra-virgin olive oil (EVOO), which is the primary source of dietary fat within the Mediterranean diet, is rich in phenolic compounds (31). The OliveNet™ library, which was previously created by our laboratory, is a curated database of 676 compounds from *Olea europaea* and 222 phenolic compounds are divided into 13 subclasses (32).

Crystal structures of the SARS-CoV-2 M^{pro} enzyme have been made available on the RCSB Protein Data Bank (PDB) and can be used for *in silico* screening (19, 26). Large ligand databases can be screened in a timely and cost-effective manner using computational methods, in an attempt to accelerate the process of drug discovery (33). The results can then be validated experimentally *in vivo* and *in vitro*. Utilising a combination of targeted molecular docking and blind docking, we aimed to identify 'hit' compounds from a selection of 300 ligands that could potentially inhibit M^{pro}. This included 211 phenolic compounds and 13 fatty acids from our OliveNet™ library, known protease inhibitors, several antibiotics for comparison and the α-ketoamide inhibitor as a control (32). Molecular dynamics (MD) simulations were

subsequently performed to evaluate the top three candidates and ultimately determine the lead compounds.

Materials and Methods

Protein structure and ligands

The crystal structure of SARS-CoV-2 M^{pro} was obtained from the RSCB Protein Data Bank (PDB ID: 6LU7) (18, 34). 300 compounds were selected for screening against M^{pro}. This comprised of 211 phenolic compounds and 13 fatty acids were sourced from the OliveNet™ Library (32), and an additional 76 ligands based on known protease inhibitors and antibiotics, as well as compounds with antiviral, anti-inflammatory, anti-parasitic, anti-malarial, antioxidant and anti-ageing properties (22, 28, 35-59). A full list of the ligands that were screened can be found in the supplementary information (Table S1). Ligand structures were obtained from the National Centre for Biotechnology Information (NCBI) PubChem database (60), or drawn using Chem3D 19.0 (Perkin Elmer, Massachusetts, USA) if they weren't available.

Docking to the active site of the SARS-CoV-2 main protease monomer

Structure preparation and molecular docking was performed using the quantum-mechanics-polarised ligand docking (QPLD) protocol of the Schrödinger Suite (version 2018-1) molecular modelling package (61-65) as previously described (66). A 20 x 20 x 20 Å receptor grid was generated centred around active site residues Thr24, Thr25, His163, Pro168 and Gly143 (19).

Compounds were also docked to the active site of M^{pro} using AutoDock Vina (67), following the processing of protein and ligand structures using PyRx (68) to generate their corresponding pdbqt files. The protein structure was assumed to be rigid, and rotatable torsions of the ligands

were activated. A receptor grid with dimensions of 25 x 25 x 25 Å was generated around the same active site residues. Docking was performed with an exhaustiveness of 128.

Docking calculations were performed on a Windows 10 workstation equipped with an Intel Core i7 (2.90 GHz) and 8.00 GB of RAM.

Blind docking to the SARS-CoV-2 main protease dimer

As the SARS-CoV-2 M^{pro} is known to function as a homodimer (18), this complex was assembled using the Proteins, Interfaces, Structures and Assemblies (PDBePISA) server (69) for blind docking to identify potential binding sites. Structures were processed in PyRx, and docking performed AutoDock Vina (67) using a receptor grid encompassing the entire protein surface at an exhaustiveness of 128. For selected top binding compounds, blind docking was also performed at an exhaustiveness of 2000 using cloud computing services provided by Galileo (Hypernet Labs).

Molecular dynamics simulations

Classical MD simulations were performed using GROMACS 2018.2 software (70, 71) with the CHARMM27 force field (72, 73) using docked ligands as starting structures as previously described (66). Ligand topologies were generated using SwissParam (74). For cyanidin-3-O-glucoside, Lennard-Jones parameters for the oxonium ion were assumed to be similar to those for the ether group (75). Simulations were performed with a time-step of 2 fs in triplicate for 100 ns.

Molecular Mechanics-Poisson Boltzmann Surface Area (MM-PBSA) was employed for the quantification of free energy calculations (76) using the g_mmpbsa tool (77), as previously described (66). Calculations were performed in triplicate on 1 ns segments, from 99 to 100 ns, of the stabilised trajectories (78).

Visual Molecular Dynamics 1.9.3 (79) was used for visualisation and analysis. Calculations were performed on a Dual Intel Xeon "Cascade Lake" Silver 4215 processor cluster (Topaz) at the Pawsey Supercomputing Centre, and an Intel Xeon E5-2650 v4 processor cluster (Spartan) hosted at the University of Melbourne (80).

Enzyme-linked immunosorbent assay

To confirm inhibition of the SARS-CoV-2 M^{pro} *in vitro*, an enzyme-linked immunosorbent assay (ELISA), was performed. The BPL 3CL protease (SARS-CoV-2) assay kit (BPS Bioscience, San Diego, CA, USA), was used, and the assay performed according to the manufacturer's instructions. The internal positive control was the broad-spectrum antiviral GC376 and was tested (n = 9 determinations), at a final concentration of 50 μM. The small molecule test inhibitors that we tested were hypericin (89%, HWI pharma services GmbH, Germany), cyanidin-3-O-glucoside (reference standard, PhytoLab, Germany), SRT2104 and SRT1720 (>99%, AdooQ® Bioscience, Irvine, CA, USA), resveratrol (>99%), and L-sulforaphane (>95%, Sigma-Aldrich, St Luis, MO, USA). The inhibitors were prepared as 20 mM stock solutions and stored at -80ºC until use. For the ELISA assay, doubling dilutions of each of the test inhibitors were performed to achieve final concentrations ranging from 0.25 to 128 μM; each concentration of the test inhibitors was assayed in triplicate. Following addition of the substrate solution the plate was read using an excitation wavelength of 360 nm and detection of emission at a wavelength of 460 nm. Fluorescence intensities were measured, and the % protease inhibition was calculated as the ratio of fluorescence intensity observed with each test inhibitor and the total activity (n = 9 determinations), taking background (n = 9 determinations) into account. The IC_{50} values for applicable test inhibitors (hypericin, cyanidin-3-O-glucoside, and SRT2104), were also calculated.

Results and Discussion

Identification of key compounds with relatively high affinity to the active site of the SARS-CoV-2 main protease

The α-ketoamide ligand (13b) was previously identified by Zhang et al. to inhibit M^{pro} with a half maximal inhibitory concentration (IC_{50}) value of 0.67 ± 0.18 μM (26). As a result, this compound was used as a control. Each protomer of the M^{pro} enzyme consists of three domains and the active site is located between domain I and domain II (19). When docked to the substrate-binding site of the crystal structure, the α-ketoamide ligand formed hydrogen bonds with the protein residues and this included Glu166, His164 and Gln189. The inhibitor was predominantly surrounded by hydrophobic and polar residues including Cys145, Asn142, Tyr54, Thr190 and Pro168 (Figure 1). The binding affinities of this compound were -65.7 and -7.7 kcal/mol in Schrödinger and AutoDock, respectively. Our lab has also recently verified the interaction of the α–ketoamide inhibitor with the active site of M^{pro} from SARS-CoV-2 (66).

The control compound was positioned in a similar site as the co-crystallised ligand (N3) (19). Previously, it has been found that the negatively charged residue Glu166 plays an important role in forming the S1 pocket of the binding site (19). The hydrophobic residue Cys145 is also involved in the mechanisms of action of N3 and the α-ketoamide inhibitor (19, 26). The Cys145 and His41 residues in the SARS-CoV-2 main protease form a catalytic dyad (19). The M^{pro} enzyme is a cysteine protease and the inhibitors specifically interact with Cys145 covalently (19, 26). Covalent docking tools have been made available however, the success of this screening approach depends on a number of factors (81, 82). This includes the contribution of non-covalent interactions and the mechanism of covalent bonding (81, 82). In the current study, conventional docking methods were used and there is evidence to suggest that noncovalent

docking is successful in elucidating the interactions that are occurring within protein-ligand complexes at the molecular level (33, 83, 84).

Drug repositioning has become one of the most important strategies for combating COVID-19 and virtual screening approaches continue to play a major role in this (85). With this in mind, 300 compounds were docked to the catalytic core of the SARS-CoV-2 M^{pro} enzyme. Out of the 300 compounds, 297 were successful in binding to the active site of the protomer using the QPLD protocol in Schrödinger and the Glide energies ranged from -16.3 to -82.0 kcal/mol. All 300 compounds were predicted to bind using AutoDock Vina and the binding affinities ranged from -3.7 to -10.7 kcal/mol. When examining the effect of molecular weight of the small molecules and when comparing the binding affinities from both programs, the correlation coefficients were found to be approximately 0.7 for both parameters (Figure S1 and S2). Previous studies have evaluated a number of molecular docking programs that are available for use and have found that Glide is more accurate in predicting the crystallographic pose of ligands (86). Therefore, the results that were generated from Schrödinger were the main focus of this section and the data from AutoDock was used for comparison (Figures S1 and S2).

In regards to the 211 phenolic compounds from the OliveNet™ database, it was evident that the flavonoid, glucoside and secoiridoid subclasses were binding strongly to the active site (Table S1). Conversely, the simple phenols, hydroxyphenylacetic acids, hydroxybenzoic acids and methoxyphenols had weaker binding affinities (Table S1). The biological activities of flavonoids have been extensively investigated over the years and there are studies that have examined the inhibitory activity of certain flavonoid compounds against the M^{pro} enzyme of SARS-CoV. This includes luteolin, tetra-O-galloyl-β-D-glucose and baicalin to name a few (30, 87, 88). Since being declared a pandemic, several papers that have assessed the ability of natural compounds to target SARS-CoV-2 proteins have been made available. In a recent study

conducted by Ul Qamar et al. *in silico* techniques were used to detect lead molecules from a medical plant library and they highlighted how their study may contribute to the development of natural antiviral agents in the future (89). Although there are hurdles that are yet to be overcome, Thomford et al. emphasise that advancements in predictive computational methods have made it possible for the properties of natural products and their derivatives to be explored and for novel therapeutic moieties to be discovered (90).

Saquinavir and ritonavir were the protease inhibitors that were binding more strongly than the α-ketoamide ligand, while nelfinavir had a similar Glide energy as the control compound. This is in accordance with a paper published by Pant et al., as their molecular docking analysis revealed that these three antivirals scored well and interacted with important residues (91). In addition to the phenolic compounds from OliveNet^{TM} and the protease inhibitors, some of the other top binding ligands included (-)-epicatechin gallate, remdesivir, D,L-sulforaphane glutathione, SRT2104, SRT1720, hypericin, curcumin, demethoxycurcumin, baricitinib and baicalin.

Based on this initial screen, 30 compounds were selected for further examination. A description of these compounds and their binding affinities can be found in Table 1. The structures of the ligands not found in the OliveNet^{TM} database are provided in the supplementary information (Table S2). Simeprevir, ivermectin and ebselen were unable to produce output structures when docked to the M^{pro} protomer through Schrödinger. These three ligands were successful in binding to the active site using AutoDock and their binding affinities were -8.5, -7.6 and -6.5 kcal/mol, respectively. When examining the protein-ligand interactions, several compounds were forming inter-atomic contacts with the residues Glu166, Asn142, His41, Gly143 and Thr26.

In order to narrow down the list and identify lead compounds, blind docking was conducted on the crystal structure of the M^{pro} dimer using the α-ketoamide 13b inhibitor and selection of 30 compounds at an exhaustiveness of 128. Overall, there were 19 ligands that had poses within the substrate-binding sites of the enzyme promoters (promoter A and promoter B). They were β-hydroxy verbascoside, ceftazidime, cyanidin-3-O-glucoside, D,L-sulforaphane glutathione, ebselen, (-)-epicatechin gallate, hypericin, indinavir, isoacteoside, nelfinavir, oxidized verbascoside, quercetin-3-O-rutinoside, quercitrin, remdesivir, saquinavir, simeprevir, SRT1720, SRT2104 and verbascoside.

Based on the results, three compounds were chosen for further study and they were hypericin, SRT2104 and cyanidin-3-O-glucoside (Figure 2). Blind docking was performed for these three compounds at an exhaustiveness of 2000. Hypericin and SRT2104 had 4 poses each within the active sites of the dimer whereas cyanidin-3-O-glucose had 7 poses (Figure 2 & Tables S3-S6). When docked to the active site of the M^{pro} monomer, these compounds were binding with relatively high affinity to the active site, with Glide energies of -51.7, -60.5 and -62.7 kcal/mol, respectively (Table 1). SRT2104 and cyanidin-3-O-glucoside formed a π–π interaction with His41 of M^{pro}, while hypericin formed a hydrogen bond with His164. Residues Asn142, Leu141, Glu166 and Thr190 were also involved in inter-atomic contacts with cyanidin-3-O-glucoside. In addition to His41, SRT2104 formed hydrogen bonds with Thr26 and Gly143 (Figure 3). Although all three compounds were positioned in a similar manner within the catalytic core, the conformations of hypericin and cyanidin-3-O-glucoside were closer to that of the α-ketoamide inhibitor.

We extended our docking studies with these compounds to include additional dimeric structures of the SARS-CoV-2 M^{pro}, including 6Y2G (92) and 6M03 (93). Our results indicate docking to these protein structures yielded similar results, with ligands consistently binding in

proximity to the key active site residues (Figure S3). It is noted that out of the top three ligands, cyanidin-3-O-glucoside consistently binds with the strongest affinity across all protease structures.

Molecular dynamic simulations highlight the stability of cyanidin-3-O-glucoside, SRT2104, and hypericin compounds with the main protease complex

To assess the stability of the ligands in complex with the main protease dimer, classical MD simulations were performed. Each system comprised of two ligands bound to the active sites on each protomer, as shown in Movies S1-4. Root mean square deviation (RMSD) analysis in Figure 4 shows that the systems reached equilibrium after 50 ns, with subsequent analysis performed after this timepoint. Analysis of RMSD during the stabilised trajectory indicated that SARS-CoV-2 M^{pro} bound to ligands yielded slightly more stable protein complexes. With an average RMSD of 0.30 nm in the apo protein, the top ligands bound to the protease complex yielded slightly lower values compared to apo: 0.27 nm for hypericin, 0.28 nm for SRT2104, and 0.25 nm for cyanidin-3-O-glucoside. Root mean square fluctuation (RMSF) was also analysed, indicating that the main fluctuations were occurring at Leu50 in domain I and at Gln189 located in the connecting loop, which are located in proximity to the active site (Figure 4). A more prominent fluctuation also occurred at residue Tyr154 in domain II. The largest fluctuation occurred at the C-terminal Gln306 across both protomers. When the RMSF values for the apo protease were subtracted from the ligand-bound values in Figure 4, peaks in residue fluctuation diminished, with the exception of the C-terminal Gln306. This indicates that the binding of hypericin, SRT2104, and cyanidin-3-O-glucoside to the active site of the protease does not influence residue fluctuation in the overall protein.

Utilising trajectory segments spanning the final nanosecond of each system in triplicate, MM-PBSA was performed to determine binding free energy, as well as residue energy contributions

to ligand binding (Figure 5). Out of the three ligands, cyanidin-3-O-glucoside demonstrated the strongest ΔG to the active site of both protomers of M^{pro}, with values of -50.8 kcal/mol in protomer A and -42.1 kcal/mol in protomer B. ΔG values of approximately -20 kcal/mol were observed for hypericin bound to both protomers of M^{pro} and for SRT2104 bound to the active site of protomer B. It is noted that SRT2104 bound to the active site of protomer A demonstrates a noticeably weaker ΔG of -8.7 kcal/mol. This is due to unbinding events occurring in two out of three replicate simulations, with one of these shown in Movie S3. Consequently, while residue energy contributions to SRT2104 binding in the active site of protomer B are confined to active site residues, energy contributions in protomer A binding are also apparent in Val72, Arg76, and Asp92 in domain I, where SRT2104 attaches towards the end of the trajectory (Movie S3).

For SRT2104 bound to protomer B and hypericin bound to the active site of both protomers of M^{pro}, the main peaks in residue energy contributions were confined to active site residues surrounding the bound ligand in its corresponding protomer. With favourable energy contributions defined as peaks below the y-axis, active site residues Met49 and Met165 were relatively consistent in producing strong favourable energy contributions ranging from -0.5 to -1.3 kcal/mol. Glu166 produced unfavourable contributions, with values of +0.8 kcal/mol for hypericin bound to protomer A, +1.0 kcal/mol to protomer B, and +0.5 kcal/mol for SRT2104 bound to the active site of protomer B.

In contrast to hypericin and SRT2104, residue energy contributions for cyanidin-3-O-glucoside demonstrates large fluctuations across the entire protein, regardless of the protomer to which the ligand is bound. Energy peaks were nevertheless present at active site residues Ser1, Asp187, and Arg188. Peaks for Glu166 across both protomers were conversely favourable contributions. While more rigorous free energy methods may be required for further investigation, the dominating favourable energy contributions yield a strong ΔG of cyanidin-

3-O-glucoside to the active site of M^{pro}, which is observed to remain stable throughout the trajectory (Movie S4).

Hypericin and cyanidin-3-O-glucoside as lead compounds for further evaluation

Cyanidin-3-O-glucoside belongs to the flavonoid subclass and is classified as an anthocyanin (94). In general, anthocyanins are water-soluble pigments and they are present in a variety of plants and fruits (94, 95). Their antioxidant, anti-inflammatory and neuroprotective properties have gained the attention of researchers and different methodologies are being trialled to assess how the bioavailability of these compounds could be increased (29, 96, 97). Pour et al. have also published a comprehensive review on the antiviral properties of anthocyanins and emphasised the need for novel drugs to be rapidly developed (29). We also identified the sirtuin 1 (SIRT1) activator SRT2104 as a potential hit ligand (98).

Furthermore, hypericin is a compound that is naturally found in the perennial plant *Hypericum perforatum* (St. John's wort) and its mechanisms of action require further elucidation (99-102). Hypericin is considered to be a potent photosensitising agent and its potential use in cancer therapy has been investigated (102). The antidepressant effects of St. John's wort have also been reported in the literature (100). Likewise, the protective properties of hypericin against enveloped and non-enveloped viruses have been explored and previous studies have focused on hepatitis C, infectious bronchitis virus and human immunodeficiency virus 1 (HIV-1) (103-108). It is important to note that drug-drug interactions have been described for hypericin and medications such as HIV protease inhibitors (109, 110). Therefore, it is imperative that the pharmacokinetics of these compounds are taken into consideration. Hypericin and cyanidin-3-O-glucoside were consequently identified as the lead dietary compounds in this study and this is also consistent with a recently published paper by Islam et al (111).

To confirm potential inhibition of the SARS-CoV-2 *in vitro*, we performed an ELISA using a commercially available 3CL protease (SARS-CoV-2) assay kit. The IC_{50} for the GC376 positive antiviral control used in this ELISA has been calculated to be 0.46 μM (as provided the kit supplier; BPS Bioscience). Our findings indicate that hypericin results in a concentration-dependent inhibition of M^{pro} activity, with an IC_{50} value calculated to be 63.6 ± 5.7 μM (Figure 6, and Table 2). Similarly, cyanidin-3-O-glucoside and SRT2104 resulted in concentration-dependent inhibition of the M^{pro} with IC_{50} values calculated to be 65.1 ± 14.6 μM and 85.0 ± 16.8 μM, respectively (Table 2). Notably, IC_{50} values for SRT1720, resveratrol and L-sulforaphane could not be determined (up to 128 μM, Table 2), consistent with the lower binding energies observed for these compounds in the *in silico* work (Table S1). Similarly, the percentage protease inhibition at 50 μM GC376 was determined to be 97.9 ± 1.8% in our experiments (n = 9 determinations, Figure 6). As shown in Table 2, the percentage protease inhibition at 50 μM for our test inhibitors was lower with 42.8 ± 8.2% and 22.6 ± 4.3% inhibition of M^{pro} activity observed for hypericin and cyanidin-3-0-glucoside, respectively. Therefore, our findings clearly highlight a distinct order of potency of GC376 (covalent inhibitor) >>> hypericin and cyanidin-3-O-glucoside > SRT2104 > SRT1720 >>> resveratrol and L-sulforaphane.

Conclusion

Overall, our *in silico* findings and *in vitr*o ELISA assay results indicate that, although not as potent as the covalent GC376 broad-spectrum antiviral, hypericin and cyandin-3-O-glucoside, may be considered as potential lead compounds as inhibitors of the SARS-CoV-2 M^{pro}. Given the considerable previous work with hypericin and cyandin-3-O-glucoside in models of disease, including previously reported antiviral effects, further investigation of these compounds in the context of COVID-19 is warranted.

Acknowledgements

We would like to acknowledge intellectual and financial support by McCord Research (Iowa, USA). JL and KKD are supported by an Australian Government Research Training Program Scholarship. We are indebted to Alfonso Perez Escudero and the team at Crowdfight COVID-19 for enabling access to supercomputing facilities, and to Matthew Gasperetti and the team at Hypernet Labs; Galileo, for enabling cloud computing for this project. We thank the National Computing Infrastructure (NCI), and the Pawsey Supercomputing Centre in Australia (funded by the Australian Government). Further, we thank the Spartan High Performance Computing service (University of Melbourne), and the Partnership for Advanced Computing in Europe (PRACE) for awarding the access to Piz Daint, hosted at the Swiss National Supercomputing Centre (CSCS), Switzerland.

Conflict of interest

Epigenomic Medicine Program (TCK) is supported financially by McCord Research (Iowa, USA), which has a financial interest in dietary compounds described in this work. However, there is no conflict of interest with respect to the inhibition of the SARS-CoV-2 main protease. The remaining co-authors also have no conflicts of interest.

References

1. Park SE. Epidemiology, virology, and clinical features of severe acute respiratory syndrome -coronavirus-2 (SARS-CoV-2; Coronavirus Disease-19). J Korean Pediatr Soc. 2020;0(0):0-.
2. World Health Organization. Novel Coronavirus (2019-nCoV): Situation Report - 1. Geneva: World Health Organization; 2020 [Available from: https://www.who.int/docs/default-source/coronaviruse/situation-reports/20200121-sitrep-1-2019-ncov.pdf.
3. Gabutti G, d'Anchera E, Sandri F, Savio M, Stefanati A. Coronavirus: update related to the current outbreak of COVID-19. Infectious Diseases and Therapy. 2020.

4. Gorbalenya AE, Baker SC, Baric RS, de Groot RJ, Drosten C, Gulyaeva AA, et al. The species severe acute respiratory syndrome-related coronavirus: classifying 2019-nCoV and naming it SARS-CoV-2. Nature Microbiology. 2020;5(4):536-44.
5. Tai W, He L, Zhang X, Pu J, Voronin D, Jiang S, et al. Characterization of the receptor-binding domain (RBD) of 2019 novel coronavirus: implication for development of RBD protein as a viral attachment inhibitor and vaccine. Cellular & Molecular Immunology. 2020.
6. World Health Organization. Novel Coronavirus (2019-nCoV): Situation Report - 22. Geneva: World Health Organization; 2020 [Available from: https://www.who.int/docs/default-source/coronaviruse/situation-reports/20200211-sitrep-22-ncov.pdf.
7. World Health Organization. Coronavirus Disease 2019 (COVID-19): Situation Report - 51. Geneva: World Health Organization; 2020 [Available from: https://www.who.int/docs/default-source/coronaviruse/situation-reports/20200311-sitrep-51-covid-19.pdf.
8. World Health Organization. Coronavirus Disease 2019 (COVID-19): Situation Report - 130. Geneva: World Health Organization; 2020 [Available from: https://www.who.int/docs/default-source/coronaviruse/situation-reports/20200529-covid-19-sitrep-130.pdf.
9. Amanat F, Krammer F. SARS-CoV-2 vaccines: status report. Immunity. 2020.
10. Chen W-H, Strych U, Hotez PJ, Bottazzi ME. The SARS-CoV-2 vaccine pipeline: an overview. Curr Trop Med Rep. 2020:1-4.
11. Rosa SGV, Santos WC. Clinical trials on drug repositioning for COVID-19 treatment. Rev Panam Salud Publica. 2020;44:e40-e.
12. Zhou Y, Hou Y, Shen J, Huang Y, Martin W, Cheng F. Network-based drug repurposing for novel coronavirus 2019-nCoV/SARS-CoV-2. Cell Discov. 2020;6:14-.
13. Yao X, Ye F, Zhang M, Cui C, Huang B, Niu P, et al. In vitro antiviral activity and projection of optimized dosing design of hydroxychloroquine for the treatment of severe acute respiratory syndrome coronavirus 2 (SARS-CoV-2). Clinical Infectious Diseases. 2020.
14. Ren J-l, Zhang A-H, Wang X-J. Traditional Chinese medicine for COVID-19 treatment. Pharmacological Research. 2020;155:104743.
15. Al-Tawfiq JA, Al-Homoud AH, Memish ZA. Remdesivir as a possible therapeutic option for the COVID-19. Travel Med Infect Dis. 2020:101615-.
16. Gautret P, Lagier J-C, Parola P, Hoang VT, Meddeb L, Mailhe M, et al. Hydroxychloroquine and azithromycin as a treatment of COVID-19: results of an open-label non-randomized clinical trial. Int J Antimicrob Agents. 2020:105949-.
17. Cao B, Wang Y, Wen D, Liu W, Wang J, Fan G, et al. A trial of lopinavir-ritonavir in adults hospitalized with severe Covid-19. N Engl J Med. 2020:NEJMoa2001282.
18. Jin Z, Du X, Xu Y, Deng Y, Liu M, Zhao Y, et al. Structure of Mpro from COVID-19 virus and discovery of its inhibitors. Nature. 2020.
19. Zhu N, Zhang D, Wang W, Li X, Yang B, Song J, et al. A novel coronavirus from patients with pneumonia in China, 2019. New England Journal of Medicine. 2020;382(8):727-33.
20. Zhou P, Yang X-L, Wang X-G, Hu B, Zhang L, Zhang W, et al. A pneumonia outbreak associated with a new coronavirus of probable bat origin. Nature. 2020;579(7798):270-3.
21. Walls AC, Park Y-J, Tortorici MA, Wall A, McGuire AT, Veesler D. Structure, function, and antigenicity of the SARS-CoV-2 spike glycoprotein. Cell. 2020.
22. Yan R, Zhang Y, Li Y, Xia L, Guo Y, Zhou Q. Structural basis for the recognition of SARS-CoV-2 by full-length human ACE2. Science. 2020;367(6485):1444.
23. Wrapp D, Wang N, Corbett KS, Goldsmith JA, Hsieh C-L, Abiona O, et al. Cryo-EM structure of the 2019-nCoV spike in the prefusion conformation. Science. 2020;367(6483):1260.

24. Pillaiyar T, Manickam M, Namasivayam V, Hayashi Y, Jung S-H. An overview of severe acute respiratory syndrome–coronavirus (SARS-CoV) 3CL protease inhibitors: peptidomimetics and small molecule chemotherapy. Journal of Medicinal Chemistry. 2016;59(14):6595-628.
25. Xue X, Yu H, Yang H, Xue F, Wu Z, Shen W, et al. Structures of two coronavirus main proteases: implications for substrate binding and antiviral drug design. Journal of Virology. 2008;82(5):2515.
26. Zhang L, Lin D, Sun X, Curth U, Drosten C, Sauerhering L, et al. Crystal structure of SARS-CoV-2 main protease provides a basis for design of improved α-ketoamide inhibitors. Science. 2020:eabb3405.
27. Denaro M, Smeriglio A, Barreca D, De Francesco C, Occhiuto C, Milano G, et al. Antiviral activity of plants and their isolated bioactive compounds: An update. Phytotherapy Research. 2020;34(4):742-68.
28. Zakaryan H, Arabyan E, Oo A, Zandi K. Flavonoids: promising natural compounds against viral infections. Arch Virol. 2017;162(9):2539-51.
29. Mohammadi Pour P, Fakhri S, Asgary S, Farzaei MH, Echeverría J. The signaling Pathways, and therapeutic targets of antiviral agents: focusing on the antiviral approaches and clinical perspectives of anthocyanins in the management of viral diseases. Front Pharmacol. 2019;10:1207-.
30. Yi L, Li Z, Yuan K, Qu X, Chen J, Wang G, et al. Small molecules blocking the entry of severe acute respiratory syndrome coronavirus into host cells. Journal of Virology. 2004;78(20):11334-9.
31. Lăcătu□u C-M, Grigorescu E-D, Floria M, Onofriescu A, Mihai B-M. The Mediterranean diet: from an environment-driven food culture to an emerging medical prescription. Int J Environ Res Public Health. 2019;16(6):942.
32. Bonvino NP, Liang J, McCord ED, Zafiris E, Benetti N, Ray NB, et al. OliveNet™: a comprehensive library of compounds from Olea europaea. Database (Oxford). 2018;2018:bay016.
33. Saikia S, Bordoloi M. Molecular docking: challenges, advances and its use in drug discovery perspective. Current Drug Targets. 2019;20(5):501-21.
34. Berman HM, Westbrook J, Feng Z, Gilliland G, Bhat TN, Weissig H, et al. The Protein Data Bank. Nucleic Acids Research. 2000;28(1):235-42.
35. Agbowuro AA, Huston WM, Gamble AB, Tyndall JDA. Proteases and protease inhibitors in infectious diseases. Medicinal Research Reviews. 2018;38(4):1295-331.
36. Agostini ML, Andres EL, Sims AC, Graham RL, Sheahan TP, Lu X, et al. Coronavirus susceptibility to the antiviral remdesivir (GS-5734) is mediated by the viral polymerase and the proofreading exoribonuclease. mBio. 2018;9(2):e00221-18.
37. Amici C, Di Caro A, Ciucci A, Chiappa L, Castilletti C, Martella V, et al. Indomethacin has a potent antiviral activity against SARS coronavirus. Antivir Ther. 2006;11(8):1021-30.
38. Chan CN, Trinité B, Levy DN. Potent inhibition of HIV-1 replication in resting CD4 T cells by resveratrol and pterostilbene. Antimicrobial Agents and Chemotherapy. 2017;61(9):e00408-17.
39. Chen H, Muhammad I, Zhang Y, Ren Y, Zhang R, Huang X, et al. Antiviral activity against infectious bronchitis virus and bioactive components of Hypericum perforatum L. 2019;10(1272).
40. Davies BE. Pharmacokinetics of oseltamivir: an oral antiviral for the treatment and prophylaxis of influenza in diverse populations. J Antimicrob Chemother. 2010;65 Suppl 2(Suppl 2):ii5-ii10.
41. Gbinigie K, Frie K. Should chloroquine and hydroxychloroquine be used to treat COVID-19? A rapid review. BJGP Open. 2020;4(2):bjgpopen20X101069.

42. Huemer HP. Possible immunosuppressive effects of drug exposure and environmental and nutritional effects on infection and vaccination. Mediators of Inflammation. 2015;2015:349176.
43. Ichikawa T, Hayashi R, Suzuki K, Imanishi S, Kambara K, Okazawa S, et al. Sirtuin 1 activator SRT1720 suppresses inflammation in an ovalbumin-induced mouse model of asthma. Respirology. 2013;18(2):332-9.
44. Khaerunnisa S, Kurniawan H, Awaluddin R, Suhartati S, Soetjipto S. Potential inhibitor of COVID-19 main protease (Mpro) from several medicinal plant compounds by molecular docking study2020.
45. Kim DE, Min JS, Jang MS, Lee JY, Shin YS, Song JH, et al. Natural bis-benzylisoquinoline alkaloids-tetrandrine, fangchinoline, and cepharanthine, inhibit human coronavirus OC43 infection of MRC-5 human lung cells. Biomolecules. 2019;9(11):696.
46. Kim JY, Kim YI, Park SJ, Kim IK, Choi YK, Kim S-H. Safe, high-throughput screening of natural compounds of MERS-CoV entry inhibitors using a pseudovirus expressing MERS-CoV spike protein. Int J Antimicrob Agents. 2018;52(5):730-2.
47. Krueger JG, Suárez-Fariñas M, Cueto I, Khacherian A, Matheson R, Parish LC, et al. A randomized, placebo-controlled study of SRT2104, a SIRT1 activator, in patients with moderate to severe psoriasis. PLOS ONE. 2015;10(11):e0142081.
48. Liang J, Mantelos A, Toh Z, Tortorella S, Ververis K, Vongsvivut J, et al. Investigation of potential anti-pneumococcal effects of l-sulforaphane and metabolites: Insights from synchrotron-FTIR microspectroscopy and molecular docking studies. Journal of Molecular Graphics and Modelling. 2020;97:107568.
49. Lin M-H, Moses DC, Hsieh C-H, Cheng S-C, Chen Y-H, Sun C-Y, et al. Disulfiram can inhibit MERS and SARS coronavirus papain-like proteases via different modes. Antiviral Res. 2018;150:155-63.
50. Lin S-C, Ho C-T, Chuo W-H, Li S, Wang TT, Lin C-C. Effective inhibition of MERS-CoV infection by resveratrol. BMC Infectious Diseases. 2017;17(1):144.
51. Lu J-W, Hsieh P-S, Lin C-C, Hu M-K, Huang S-M, Wang Y-M, et al. Synergistic effects of combination treatment using EGCG and suramin against the chikungunya virus. Biochemical and Biophysical Research Communications. 2017;491(3):595-602.
52. Moghadamtousi SZ, Kadir HA, Hassandarvish P, Tajik H, Abubakar S, Zandi K. A review on antibacterial, antiviral, and antifungal activity of curcumin. Biomed Res Int. 2014;2014:186864-.
53. Moghaddam E, Teoh B-T, Sam S-S, Lani R, Hassandarvish P, Chik Z, et al. Baicalin, a metabolite of baicalein with antiviral activity against dengue virus. Scientific Reports. 2014;4(1):5452.
54. Mohammadi Pour P, Fakhri S, Asgary S, Farzaei MH, Echeverría J. The signaling pathways, and therapeutic targets of antiviral agents: focusing on the antiviral approaches and clinical perspectives of anthocyanins in the management of viral diseases. Frontiers in Pharmacology. 2019;10(1207).
55. Richardson P, Griffin I, Tucker C, Smith D, Oechsle O, Phelan A, et al. Baricitinib as potential treatment for 2019-nCoV acute respiratory disease. The Lancet. 2020;395(10223):e30-e1.
56. Rogosnitzky M, Okediji P, Koman I. Cepharanthine: a review of the antiviral potential of a Japanese-approved alopecia drug in COVID-19. Pharmacological Reports. 2020.
57. Vankadari N. Arbidol: A potential antiviral drug for the treatment of SARS-CoV-2 by blocking trimerization of the spike glycoprotein. Int J Antimicrob Agents. 2020;56(2):105998-.
58. Zhou H, Fang Y, Xu T, Ni W-J, Shen A-Z, Meng X-M. Potential therapeutic targets and promising drugs for combating SARS-CoV-2. Br J Pharmacol. 2020;177(14):3147-61.

59. Zhou Y, Hou Y, Shen J, Huang Y, Martin W, Cheng F. Network-based drug repurposing for novel coronavirus 2019-nCoV/SARS-CoV-2. Cell Discovery. 2020;6(1):14.
60. Kim S, Chen J, Cheng T, Gindulyte A, He J, He S, et al. PubChem 2019 update: improved access to chemical data. Nucleic Acids Research. 2019;47(D1):D1102-D9.
61. Maestro. Schrödinger Release 2018-1 ed. New York, NY: Schrödinger, LLC; 2018.
62. Madhavi Sastry G, Adzhigirey M, Day T, Annabhimoju R, Sherman W. Protein and ligand preparation: parameters, protocols, and influence on virtual screening enrichments. Journal of Computer-Aided Molecular Design. 2013;27(3):221-34.
63. Dong E, Du H, Gardner L. An interactive web-based dashboard to track COVID-19 in real time. Lancet Infect Dis. 2020;20(5):533-4.
64. Phua J, Weng L, Ling L, Egi M, Lim CM, Divatia JV, et al. Intensive care management of coronavirus disease 2019 (COVID-19): challenges and recommendations. Lancet Respir Med. 2020;8(5):506-17.
65. Cho AE, Guallar V, Berne BJ, Friesner R. Importance of accurate charges in molecular docking: Quantum mechanical/molecular mechanical (QM/MM) approach. Journal of Computational Chemistry. 2005;26(9):915-31.
66. Liang J, Pitsillou E, Karagiannis C, Darmawan KK, Ng K, Hung A, et al. Interaction of the prototypical α-ketoamide inhibitor with the SARS-CoV-2 main protease active site in silico: Molecular dynamic simulations highlight the stability of the ligand-protein complex. Computational Biology and Chemistry. 2020:107292.
67. Trott O, Olson AJ. AutoDock Vina: improving the speed and accuracy of docking with a new scoring function, efficient optimization, and multithreading. Journal of Computational Chemistry. 2010;31(2):455-61.
68. Dallakyan S, Olson AJ. Small-molecule library screening by docking with PyRx. Methods Mol Biol. 2015;1263:243-50.
69. Krissinel E, Henrick K. Protein interfaces, surfaces and assemblies service PISA at European Bioinformatics Institute. J Mol Biol. 2007;372:774-97.
70. Berendsen HJC, van der Spoel D, van Drunen R. GROMACS: A message-passing parallel molecular dynamics implementation. Computer Physics Communications. 1995;91(1):43-56.
71. Abraham MJ, Murtola T, Schulz R, Páll S, Smith JC, Hess B, et al. GROMACS: High performance molecular simulations through multi-level parallelism from laptops to supercomputers. SoftwareX. 2015;1-2:19-25.
72. Bjelkmar P, Larsson P, Cuendet MA, Hess B, Lindahl E. Implementation of the CHARMM Force Field in GROMACS: Analysis of Protein Stability Effects from Correction Maps, Virtual Interaction Sites, and Water Models. Journal of Chemical Theory and Computation. 2010;6(2):459-66.
73. Vanommeslaeghe K, Hatcher E, Acharya C, Kundu S, Zhong S, Shim J, et al. CHARMM General Force Field (CGenFF): A force field for drug-like molecules compatible with the CHARMM all-atom additive biological force fields. Journal of computational chemistry. 2010;31(4):671-90.
74. Zoete V, Cuendet MA, Grosdidier A, Michielin O. SwissParam: a fast force field generation tool for small organic molecules. Journal of computational chemistry. 2011;32(11):2359-68.
75. Sagnella DE, Voth GA. Structure and dynamics of hydronium in the ion channel gramicidin A. Biophysical journal. 1996;70(5):2043-51.
76. Baker NA, Sept D, Joseph S, Holst MJ, McCammon JA. Electrostatics of nanosystems: Application to microtubules and the ribosome. Proceedings of the National Academy of Sciences. 2001;98(18):10037-41.

77. Kumari R, Kumar R, Lynn A. g_mmpbsa—A GROMACS Tool for High-Throughput MM-PBSA Calculations. Journal of chemical information and modeling. 2014;54(7):1951-62.
78. Hou T, Wang J, Li Y, Wang W. Assessing the Performance of the MM/PBSA and MM/GBSA Methods. 1. The Accuracy of Binding Free Energy Calculations Based on Molecular Dynamics Simulations. Journal of chemical information and modeling. 2011;51(1):69-82.
79. Humphrey W, Dalke A, Schulten K. VMD: visual molecular dynamics. Journal of molecular graphics. 1996;14(1):33-8, 27-8.
80. Bernard M, Lev L, Greg S, Daniel T. Spartan HPC-Cloud Hybrid: Delivering Performance and Flexibility2017.
81. Carlesso A, Chintha C, Gorman AM, Samali A, Eriksson LA. Merits and pitfalls of conventional and covalent docking in identifying new hydroxyl aryl aldehyde like compounds as human IRE1 inhibitors. Scientific Reports. 2019;9(1):3407.
82. Scarpino A, Ferenczy GG, Keserű GM. Comparative evaluation of covalent docking tools. Journal of Chemical Information and Modeling. 2018;58(7):1441-58.
83. Meng X-Y, Zhang H-X, Mezei M, Cui M. Molecular docking: a powerful approach for structure-based drug discovery. Curr Comput Aided Drug Des. 2011;7(2):146-57.
84. Wang Z, Sun H, Yao X, Li D, Xu L, Li Y, et al. Comprehensive evaluation of ten docking programs on a diverse set of protein–ligand complexes: the prediction accuracy of sampling power and scoring power. Physical Chemistry Chemical Physics. 2016;18(18):12964-75.
85. Ahn D-G, Shin H-J, Kim M-H, Lee S, Kim H-S, Myoung J, et al. Current status of epidemiology, diagnosis, therapeutics, and vaccines for novel Coronavirus Disease 2019 (COVID-19). J Microbiol Biotechnol. 2020;30(3):313-24.
86. Perola E, Walters WP, Charifson PS. A detailed comparison of current docking and scoring methods on systems of pharmaceutical relevance. Proteins. 2004;56(2):235-49.
87. Chen F, Chan KH, Jiang Y, Kao RYT, Lu HT, Fan KW, et al. In vitro susceptibility of 10 clinical isolates of SARS coronavirus to selected antiviral compounds. J Clin Virol. 2004;31(1):69-75.
88. Peiris JSM, Guan Y, Yuen KY. Severe acute respiratory syndrome. Nature Medicine. 2004;10(12):S88-S97.
89. Ul Qamar MT, Alqahtani SM, Alamri MA, Chen L-L. Structural basis of SARS-CoV-2 3CL(pro) and anti-COVID-19 drug discovery from medicinal plants. J Pharm Anal. 2020:10.1016/j.jpha.2020.03.009.
90. Thomford NE, Senthebane DA, Rowe A, Munro D, Seele P, Maroyi A, et al. Natural products for drug discovery in the 21st century: innovations for novel drug discovery. Int J Mol Sci. 2018;19(6):1578.
91. Pant S, Singh M, Ravichandiran V, Murty USN, Srivastava HK. Peptide-like and small-molecule inhibitors against Covid-19. J Biomol Struct Dyn. 2020:1-10.
92. Zhang L, Lin D, Sun X, Curth U, Drosten C, Sauerhering L, et al. Crystal structure of SARS-CoV-2 main protease provides a basis for design of improved alpha-ketoamide inhibitors. Science. 2020;368(6489):409-12.
93. Zhang B, Zhao, Y., Jin, Z., Liu, X., Yang, H., Rao, Z. The crystal structure of COVID-19 main protease in apo form: 10.2210/pdb6M03/pdb; 2020.
94. Wongwichai T, Teeyakasem P, Pruksakorn D, Kongtawelert P, Pothacharoen P. Anthocyanins and metabolites from purple rice inhibit IL-1β-induced matrix metalloproteinases expression in human articular chondrocytes through the NF-κB and ERK/MAPK pathway. Biomedicine & Pharmacotherapy. 2019;112:108610.

95. Díaz-Mula HM, Tomás-Barberán FA, García-Villalba R. Pomegranate fruit and juice (cv. Mollar), rich in ellagitannins and anthocyanins, also provide a significant content of a wide range of proanthocyanidins. Journal of Agricultural and Food Chemistry. 2019;67(33):9160-7.
96. Amin FU, Shah SA, Badshah H, Khan M, Kim MO. Anthocyanins encapsulated by PLGA@PEG nanoparticles potentially improved its free radical scavenging capabilities via p38/JNK pathway against Aβ(1-42)-induced oxidative stress. J Nanobiotechnology. 2017;15(1):12-.
97. Pojer E, Mattivi F, Johnson D, Stockley CS. The case for anthocyanin consumption to promote human health: a review. Comprehensive Reviews in Food Science and Food Safety. 2013;12(5):483-508.
98. Hoffmann E, Wald J, Lavu S, Roberts J, Beaumont C, Haddad J, et al. Pharmacokinetics and tolerability of SRT2104, a first-in-class small molecule activator of SIRT1, after single and repeated oral administration in man. Br J Clin Pharmacol. 2013;75(1):186-96.
99. Barnes J, Anderson LA, Phillipson JD. St John's wort (Hypericum perforatum L.): a review of its chemistry, pharmacology and clinical properties. Journal of Pharmacy and Pharmacology. 2001;53(5):583-600.
100. Schmidt M, Butterweck V. The mechanisms of action of St. John's wort: an update. Wiener Medizinische Wochenschrift. 2015;165(11):229-35.
101. Brockmann H, Haschad MN, Maier K, Pohl F. Über das Hypericin, den photodynamisch wirksamen Farbstoff aus Hypericum perforatum. Naturwissenschaften. 1939;27(32):550-.
102. Jendželovská Z, Jendželovský R, Kuchárová B, Fedoročko P. Hypericin in the light and in the dark: two sides of the same coin. Frontiers in Plant Science. 2016;7(560).
103. Hudson JB, Harris L, Towers GHN. The importance of light in the anti-HIV effect of hypericin. Antiviral Research. 1993;20(2):173-8.
104. Shih C-M, Wu C-H, Wu W-J, Hsiao Y-M, Ko J-L. Hypericin inhibits hepatitis C virus replication via deacetylation and down-regulation of heme oxygenase-1. Phytomedicine. 2018;46:193-8.
105. Chen H, Feng R, Muhammad I, Abbas G, Zhang Y, Ren Y, et al. Protective effects of hypericin against infectious bronchitis virus induced apoptosis and reactive oxygen species in chicken embryo kidney cells. Poult Sci. 2019;98(12):6367-77.
106. Jacobson JM, Feinman L, Liebes L, Ostrow N, Koslowski V, Tobia A, et al. Pharmacokinetics, safety, and antiviral effects of hypericin, a derivative of St. John's wort plant, in patients with chronic hepatitis C virus infection. Antimicrob Agents Chemother. 2001;45(2):517-24.
107. Chen H, Muhammad I, Zhang Y, Ren Y, Zhang R, Huang X, et al. Antiviral activity against infectious bronchitis virus and bioactive components of Hypericum perforatum L. Front Pharmacol. 2019;10(1272).
108. Tang J, Colacino JM, Larsen SH, Spitzer W. Virucidal activity of hypericin against enveloped and non-enveloped DNA and RNA viruses. Antiviral Research. 1990;13(6):313-25.
109. Patel J, Buddha B, Dey S, Pal D, Mitra A. In vitro interaction of the HIV protease inhibitor ritonavir with herbal constituents: changes in P-gp and CYP3A4 activity. American Journal of Therapeutics. 2004;11:262-77.
110. Murtaza G, Ullah N, Mukhtar F, Nawazish S, Muneer S, Mariam. Phytotherapeutics: the emerging role of intestinal and hepatocellular transporters in dug interactions with botanical supplements. Molecules. 2017;22(10):1699.
111. Islam R, Parves MR, Paul AS, Uddin N, Rahman MS, Mamun AA, et al. A molecular modeling approach to identify effective antiviral phytochemicals against the main protease of SARS-CoV-2. Journal of Biomolecular Structure and Dynamics. 2020:1-12.

Figure legends

Figure 1. Structure of the SARS-CoV-2 M^{pro} dimer in complex with the α-ketoamide 13b ligand within the substrate-binding site. M^{pro} consists of three domains, with the catalytic core located between domains I and II. Catalytic dyad residues His41 and Cys145 are highlighted in orange, and the α-ketoamide 13b ligand is shown in grey. The α-ketoamide 13b was docked to the catalytic core using the QPLD protocol of Glide, and interactions with residues are depicted. Hydrogen bonds are shown as dashed yellow lines. Hydrophobic residues are green, polar uncharged residues are cyan, and negatively charged residues are shown in red.

Figure 2. Blind docking and docking of hypericin, SRT2104, and cyanidin-3-O-glucoside to the active site of the SARS-CoV-2 M^{pro} dimer. Blind docking was performed using AutoDock Vina to produce 20 poses. Catalytic dyad residues His41 and Cys145 are highlighted in orange. Docking to the active site was performed using the QPLD protocol of Glide to each protomer of the M^{pro} dimer.

Figure 3. Residue interactions between the M^{pro} monomer and hypericin, SRT2104, and cyanidin-3-O-glucoside at 4.0 Å. Hydrogen bonds and π–π interactions are depicted by the yellow and cyan lines, respectively. The green residues are hydrophobic, the cyan residues are polar, and the red residues are negatively charged.

Figure 4: Stability of SARS-CoV-2 M^{pro} complex in the presence of hypericin, SRT2104, and cyanidin-3-O-glucoside. The protein-ligand complexes comprised of a single compound bound to the active site of each protomer of M^{pro}, with cyanidin-3-O-glucoside depicted in purple (A) as an example. Average root mean square deviation (RMSD) for protein fit to backbone (B) for 100 ns, and average root mean square fluctuation of whole protein (C) following stabilisation. (D) shows the RMSF values the apo form subtracted from ligand bound

forms of the protein. For the graphs (B – D), M^{pro} in its apo form is shown in blue. M^{pro} bound to hypericin, SRT2104, and cyanidin-3-O-glucoside is shown in red, green, and purple respectively.

Figure 5: Average energy contributions from MM-PBSA analysis were decomposed into a per-residue basis for binding of SARS-CoV-2 M^{pro} with A) hypericin, B) SRT2104, and C) cyanidin-3-O-glucoside to the active site in protomer A (blue), and active site of protomer B (purple). Energy contributions were calculated in triplicate on 1000 ps segments of stabilised trajectories.

Figure 6: Concentration-dependent inhibition of the SARS-CoV-2 M^{pro} by hypericin. To confirm *in vitro* inhibition, a 3CL protease ELISA assay was performed and fluorescence intensities at an emission of wavelength of 460 nm for concentrations of hypericin up to 128 μM (doubling dilutions), were measured. The average background (n = 9 determinations), total enzymatic activity (n = 9 determinations), and inhibition by the covalent internal positive control, GC376 at 50 μM (n = 9 determinations), are highlighted (horizontal dashed lines). Hypericin was assayed in triplicate (closed circles) and the average ± SEM values are depicted.

Figure 1

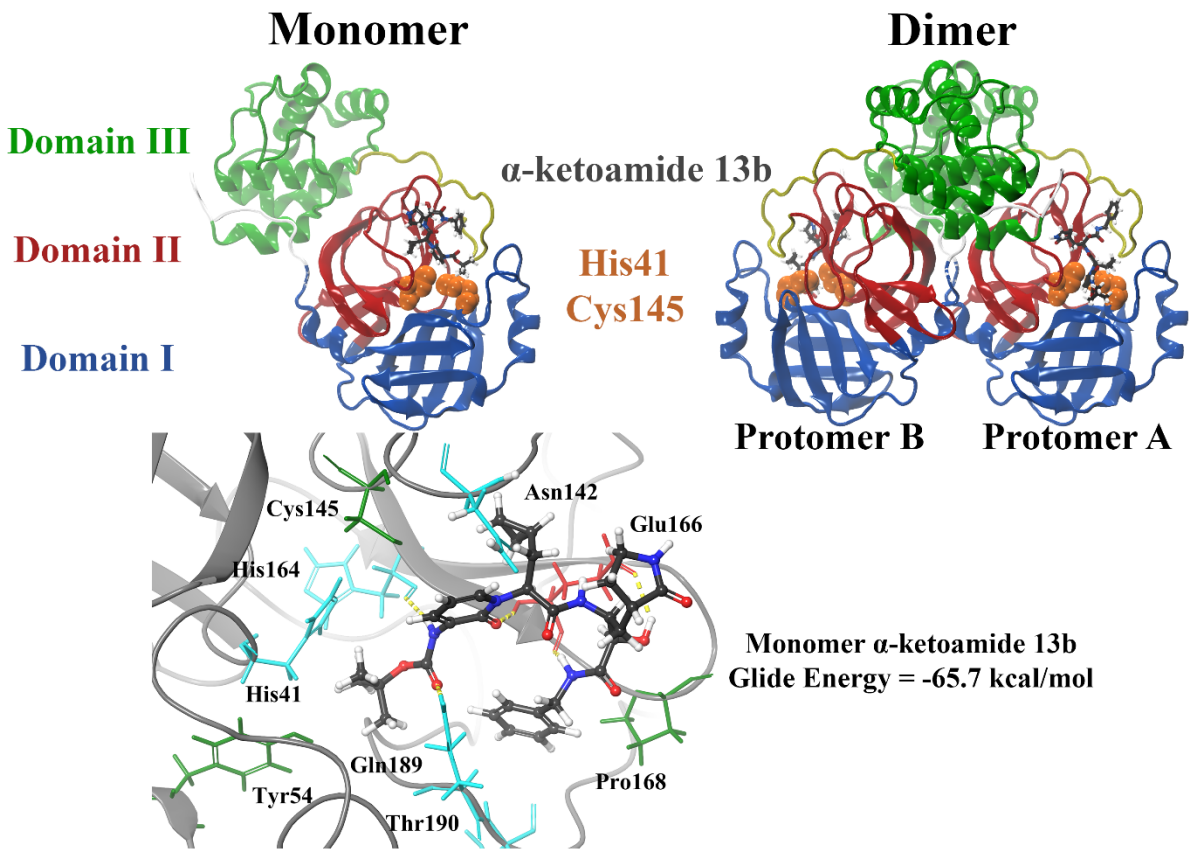
Monomer
Dimer
Domain III
Domain II
Domain I
α-ketoamide 13b
His41
Cys145
Protomer B
Protomer A
Cys145
Asn142
Glu166
His164
His41
Gln189
Tyr54
Thr190
Pro168
Monomer α-ketoamide 13b
Glide Energy = -65.7 kcal/mol

Figure 2

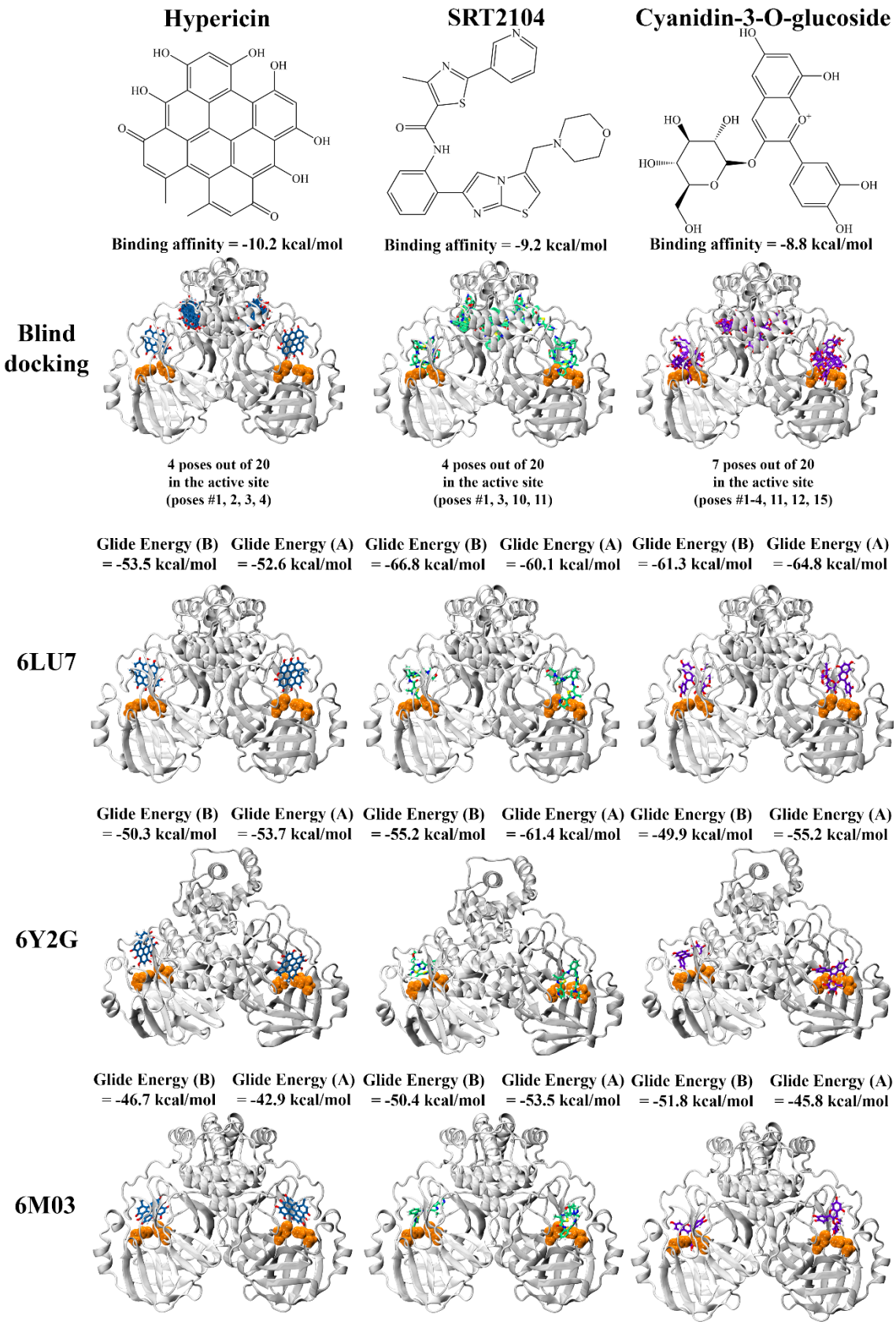
Hypericin
SRT2104
Cyanidin-3-O-glucoside
Binding affinity = -10.2 kcal/mol
Binding affinity = -9.2 kcal/mol
Binding affinity = -8.8 kcal/mol
Blind docking
4 poses out of 20 in the active site (poses #1, 2, 3, 4)
4 poses out of 20 in the active site (poses #1, 3, 10, 11)
7 poses out of 20 in the active site (poses #1-4, 11, 12, 15)
Glide Energy (B) = -53.5 kcal/mol
Glide Energy (A) = -52.6 kcal/mol
Glide Energy (B) = -66.8 kcal/mol
Glide Energy (A) = -60.1 kcal/mol
Glide Energy (B) = -61.3 kcal/mol
Glide Energy (A) = -64.8 kcal/mol
6LU7
Glide Energy (B) = -50.3 kcal/mol
Glide Energy (A) = -53.7 kcal/mol
Glide Energy (B) = -55.2 kcal/mol
Glide Energy (A) = -61.4 kcal/mol
Glide Energy (B) = -49.9 kcal/mol
Glide Energy (A) = -55.2 kcal/mol
6Y2G
Glide Energy (B) = -46.7 kcal/mol
Glide Energy (A) = -42.9 kcal/mol
Glide Energy (B) = -50.4 kcal/mol
Glide Energy (A) = -53.5 kcal/mol
Glide Energy (B) = -51.8 kcal/mol
Glide Energy (A) = -45.8 kcal/mol
6M03

Figure 3

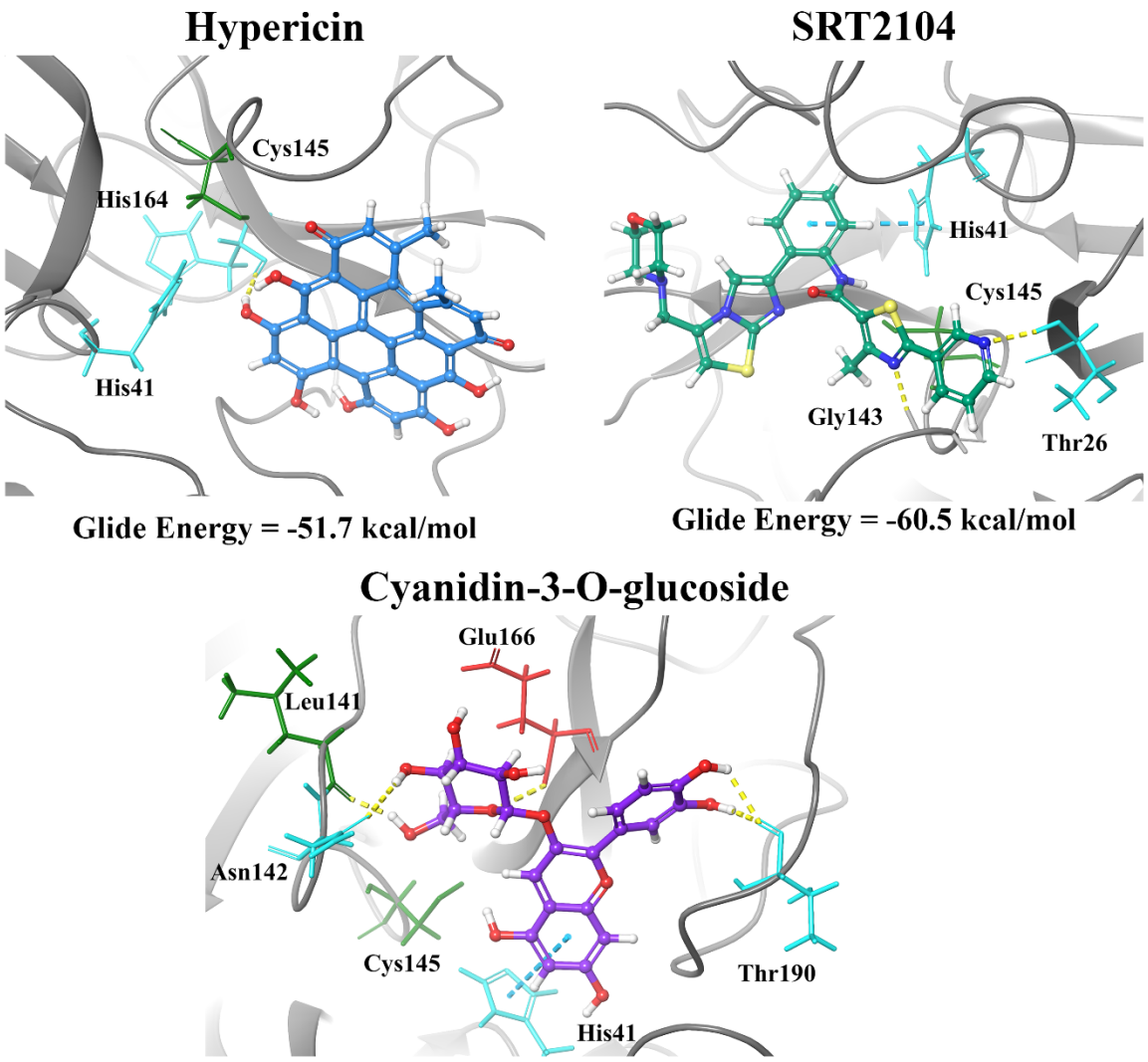
Hypericin
Cys145
His164
His41
Glide Energy = -51.7 kcal/mol
SRT2104
His41
Cys145
Gly143
Thr26
Glide Energy = -60.5 kcal/mol
Cyanidin-3-O-glucoside
Glu166
Leu141
Asn142
Cys145
Thr190
His41
Glide Energy = -62.7 kcal/mol

Figure 4

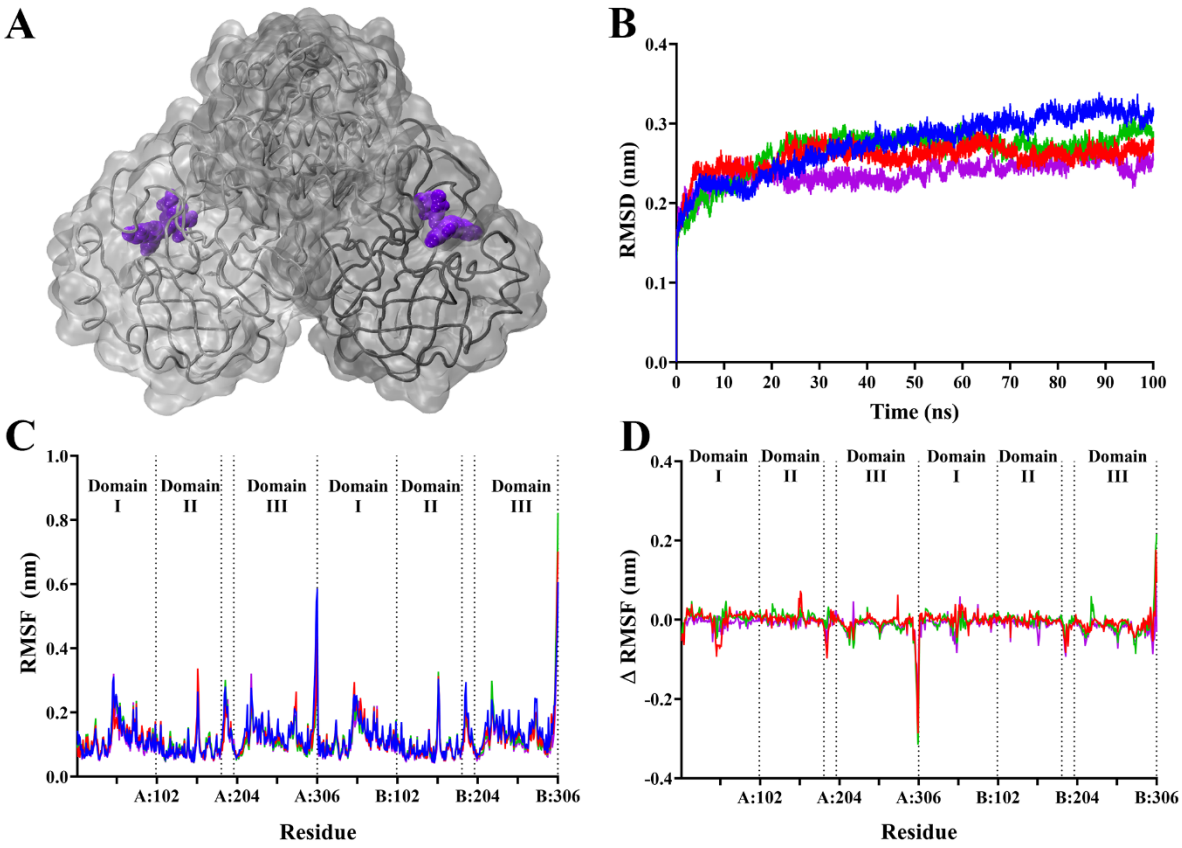
A
B
RMSD (nm)
Time (ns)
C
RMSF (nm)
Domain I
Domain II
Domain III
Domain I
Domain II
Domain III
A:102
A:204
A:306
B:102
B:204
B:306
Residue
D
Δ RMSF (nm)
Residue

Figure 5

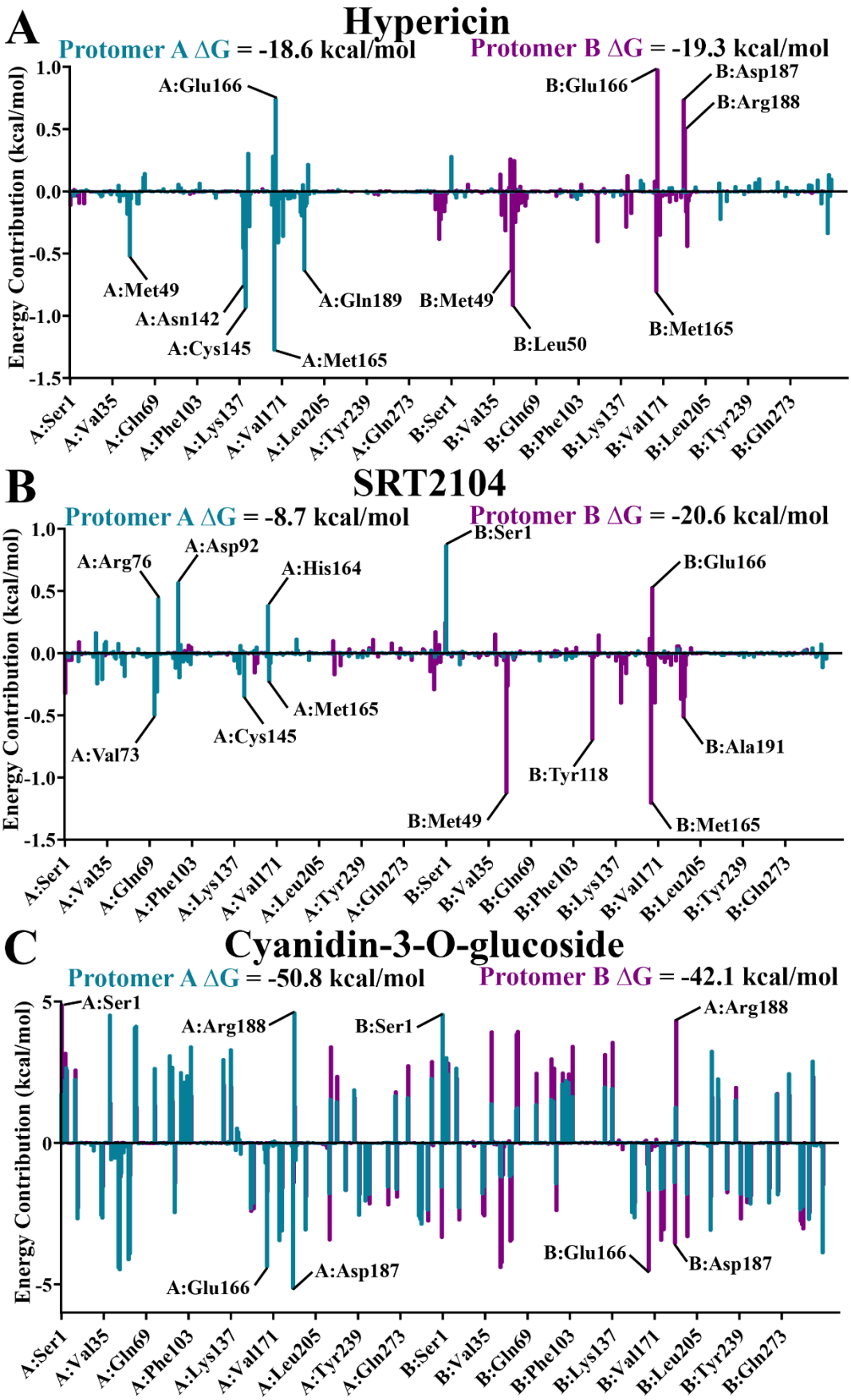
A
Hypericin
Protomer A ΔG = -18.6 kcal/mol
Protomer B ΔG = -19.3 kcal/mol
Energy Contribution (kcal/mol)
A:Glu166
A:Met49
A:Asn142
A:Cys145
A:Gln189
A:Met165
B:Glu166
B:Asp187
B:Arg188
B:Met49
B:Leu50
B:Met165
B
SRT2104
Protomer A ΔG = -8.7 kcal/mol
Protomer B ΔG = -20.6 kcal/mol
A:Arg76
A:Asp92
A:His164
A:Val73
A:Cys145
A:Met165
B:Ser1
B:Glu166
B:Tyr118
B:Ala191
B:Met49
B:Met165
C
Cyanidin-3-O-glucoside
Protomer A ΔG = -50.8 kcal/mol
Protomer B ΔG = -42.1 kcal/mol
A:Ser1
A:Arg188
B:Ser1
A:Glu166
A:Asp187
B:Glu166
B:Asp187
A:Ser1 A:Val35 A:Gln69 A:Phe103 A:Lys137 A:Val171 A:Leu205 A:Tyr239 A:Gln273 B:Ser1 B:Val35 B:Gln69 B:Phe103 B:Lys137 B:Val171 B:Leu205 B:Tyr239 B:Gln273

Figure 6

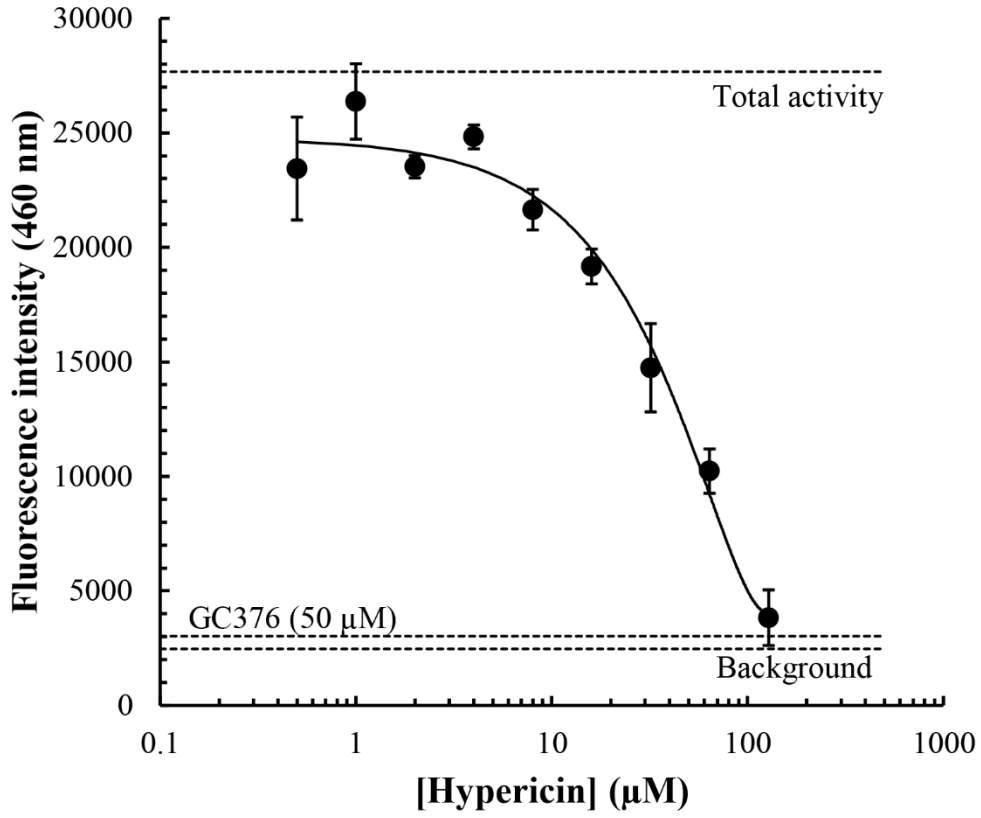
30000
25000
20000
15000
10000
5000
0
Fluorescence intensity (460 nm)
Total activity
GC376 (50 μM)
Background
0.1
1
10
100
1000
[Hypericin] (μM)

Table 1. Binding affinities (kcal/mol) of the compounds that were selected for further investigation.

Compound	Classification	Glide energies (kcal/mol)
Ritonavir	Protease inhibitor	-71.5
Saquinavir	Protease inhibitor	-77.7
Lopinavir	Protease inhibitor	-56.2
Indinavir	Protease inhibitor	-52.0
Nelfinavir	Protease inhibitor	-65.2
Darunavir	Protease inhibitor	-58.2
Remdesivir	Nucleotide analog	-58.0
Amikacin	Antibiotic	-64.5
Ceftazidime	Antibiotic	-60.5
Baricitinib	Janus kinase inhibitor	-48.8
Suramin	Antiparasitic	-66.3
Hypericin	Anthraquinone derivative	-51.7
SRT2104	Sirtuin activator	-60.5
SRT1720	Sirtuin activator	-60.5
D,L-Sulforaphane glutathione	Isothiocyanate analog	-61.7
(-)-Epicatechin gallate	Natural flavonoid compound	-64.1
Quercitrin	OliveNet™	-60.7
β-Hydroxy verbascoside	OliveNet™	-71.1
β-Hydroxy acteoside	OliveNet™	-67.7
Isoacteoside	OliveNet™	-75.1
Verbascoside	OliveNet™	-76.3
Oxidized verbascoside	OliveNet™	-71.2
Quercetin 3-O-rutinoside	OliveNet™	-77.0
Hesperidin	OliveNet™	-64.0
Rutin	OliveNet™	-69.3
Luteolin-7,4-O-diglucoside	OliveNet™	-66.3
Cyanidin-3-O-glucoside	OliveNet™	-62.7

Table 2. Inhibition of M^{pro} activity by small molecules. Percentage inhibition at a ligand concentration of 50 µM and IC_{50} values calculated using an ELISA

Compound	**IC_{50} (µM)** **Average ± SEM**	**% Protease inhibition at 50 µM ligand concentration**
Hypericin	63.6 ± 5.7	42.8 ± 8.2
Cyanidin-3-0-glucoside	65.1 ± 14.6	22.6 ± 4.3
SRT2104	85.0 ± 16.8	19.4 ± 6.4
SRT1720	NA*	9.3 ± 2.2
Resveratrol	NA*	1.8 ± 0.9
L-sulforaphane	NA*	8.4 ± 2.7

* Compound concentrations of up to 128µM were used in our experiments; the IC_{50} could not be reached for the ligands noted.

Supplementary Materials

Figure S1: Correlation of Schrödinger QM-PLD Glide Energy scores with the molecular weight of the 300 compounds that were used in the initial screen.

Figure S2: Correlation between Schrödinger QM-PLD Glide Energy scores and binding affinity scores from Autodock Vina for the 300 compounds that were used in the initial screen.

Figure S3: Comparison between docking to the active site of SARS-CoV-2 M^{pro} structures (PDB ID: 6LU7, 6Y2G, and 6M03) in protomers A and B. Hydrogen bonds are shown as yellow, pi-pi stacking in blue, and pi-cation bonds in green dashed lines.

Table S1: List of the 300 compounds that were used in this *in silico* study. Their binding affinities from Schrödinger (Glide Energy) and AutoDock (Binding Affinity) are provided.

Table S2: The structures of the 27 compounds that were predicted by the Schrödinger program to bind to the active site of the M^{pro} monomer and were selected to undergo blind docking on the M^{pro} dimer are provided.

Table S3: The blind docking results from AutoDock Vina are provided for the α-ketoamide inhibitor.

Table S4: The blind docking results from AutoDock Vina are provided for hypericin.

Table S5: The blind docking results from AutoDock Vina are provided for cyanidin-3-O-glucoside.

Table S6: The blind docking results from AutoDock Vina are provided for SRT2104.

Movie S1. 100 ns trajectory of the apo form of the SARS-CoV-2 main protease

Movie S2. 100 ns trajectory of hypericin bound to the active site of the SARS-CoV-2 main protease

Movie S3. 100 ns trajectory of SRT2104 bound to the active site of the SARS-CoV-2 main protease

Movie S4. 100 ns trajectory of cyanidin-3-O-glucoside bound to the active site of the SARS-CoV-2 main protease

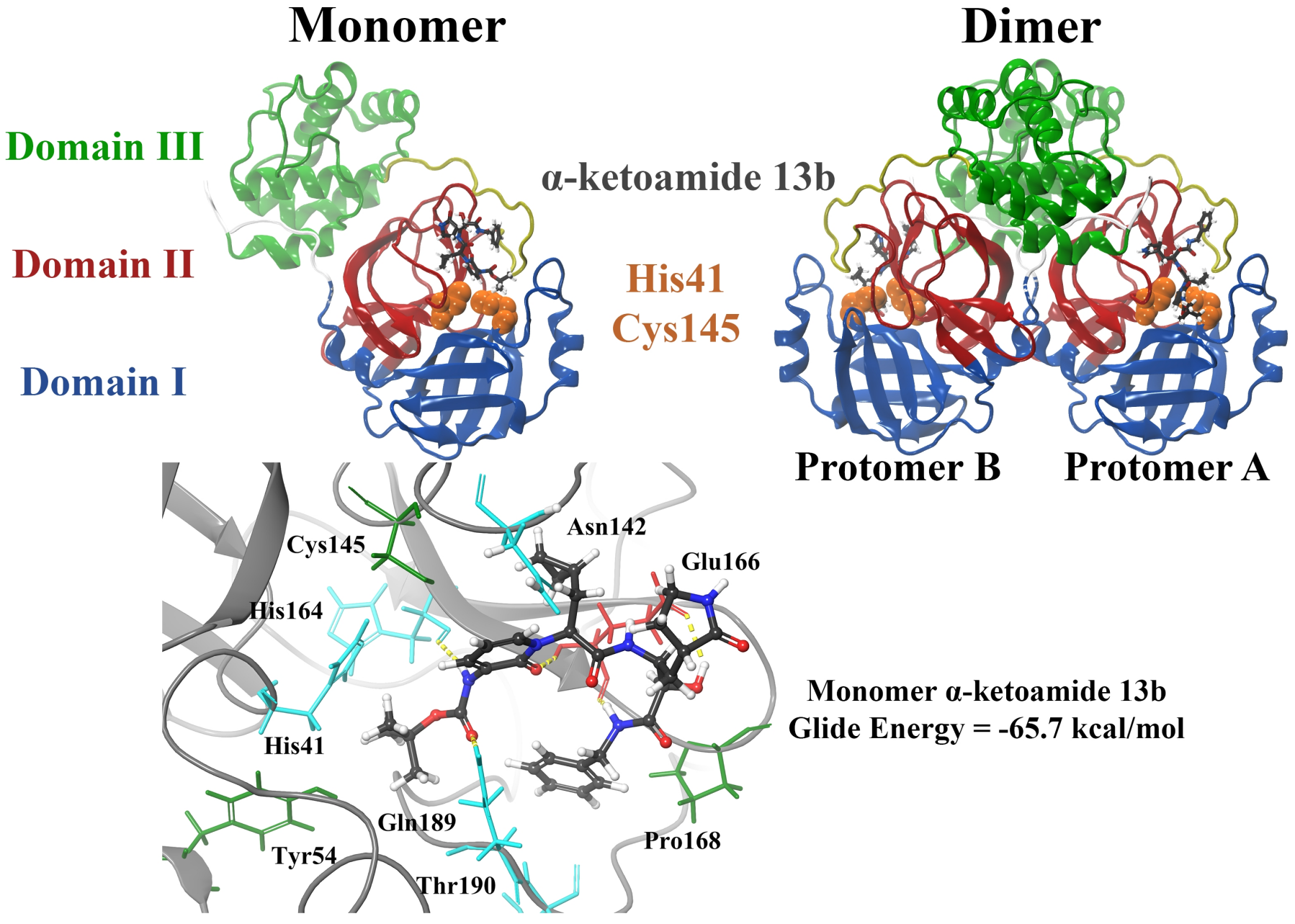
Monomer
Dimer
Domain III
Domain II
Domain I
α-ketoamide 13b
His41
Cys145
Protomer B
Protomer A
Cys145
Asn142
Glu166
His164
His41
Gln189
Tyr54
Thr190
Pro168
Monomer α-ketoamide 13b
Glide Energy = -65.7 kcal/mol

	Hypericin	SRT2104	Cyanidin-3-O-glucoside
	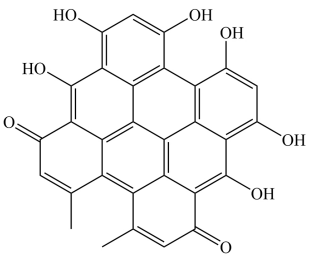	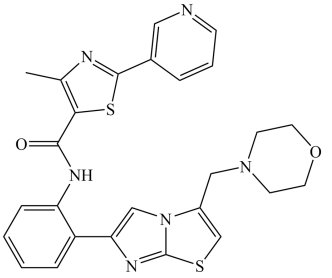	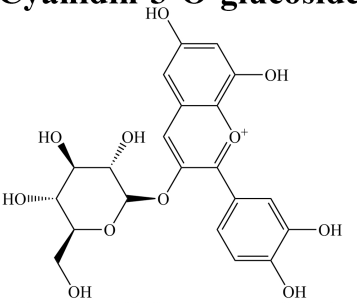
	Binding affinity = -10.2 kcal/mol	**Binding affinity = -9.2 kcal/mol**	**Binding affinity = -8.8 kcal/mol**
Blind docking	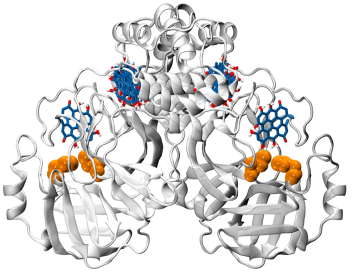	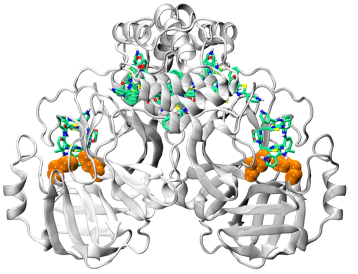	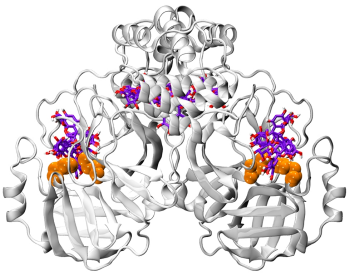
	4 poses out of 20 in the active site (poses #1, 2, 3, 4)	**4 poses out of 20 in the active site (poses #1, 3, 10, 11)**	**7 poses out of 20 in the active site (poses #1-4, 11, 12, 15)**
	Glide Energy (B) = -53.5 kcal/mol **Glide Energy (A) = -52.6 kcal/mol**	**Glide Energy (B) = -66.8 kcal/mol** **Glide Energy (A) = -60.1 kcal/mol**	**Glide Energy (B) = -61.3 kcal/mol** **Glide Energy (A) = -64.8 kcal/mol**
6LU7	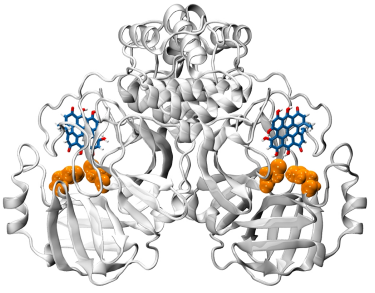	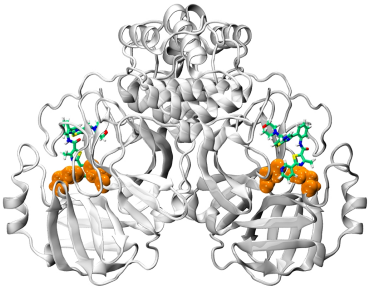	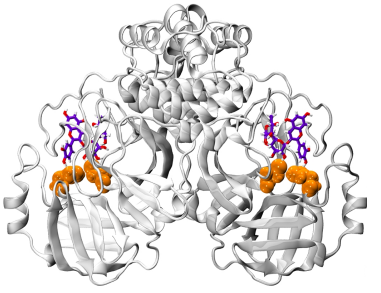
	Glide Energy (B) = -50.3 kcal/mol **Glide Energy (A) = -53.7 kcal/mol**	**Glide Energy (B) = -55.2 kcal/mol** **Glide Energy (A) = -61.4 kcal/mol**	**Glide Energy (B) = -49.9 kcal/mol** **Glide Energy (A) = -55.2 kcal/mol**
6Y2G	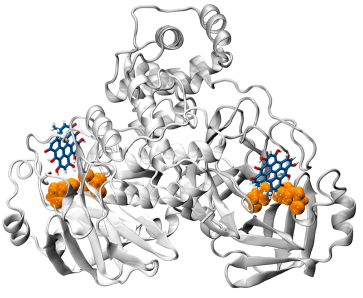	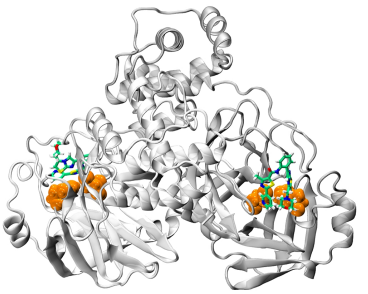	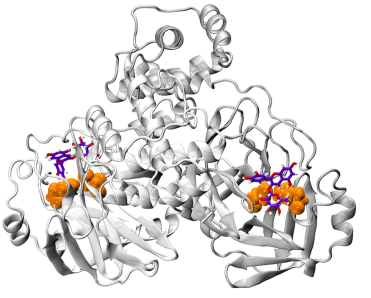
	Glide Energy (B) = -46.7 kcal/mol **Glide Energy (A) = -42.9 kcal/mol**	**Glide Energy (B) = -50.4 kcal/mol** **Glide Energy (A) = -53.5 kcal/mol**	**Glide Energy (B) = -51.8 kcal/mol** **Glide Energy (A) = -45.8 kcal/mol**
6M03	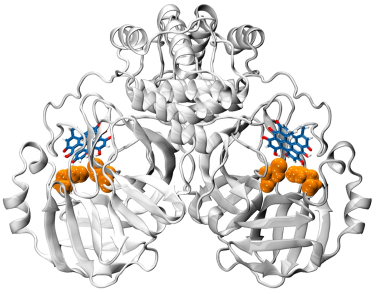	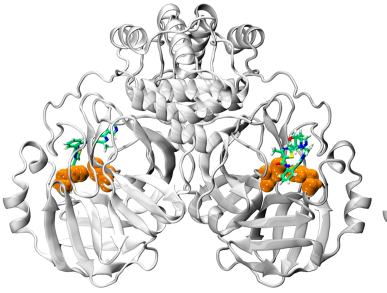	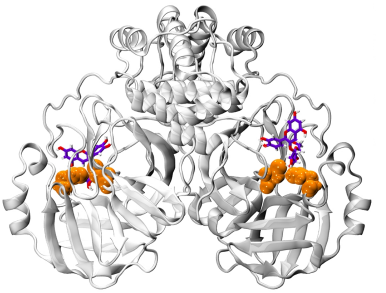

Hypericin

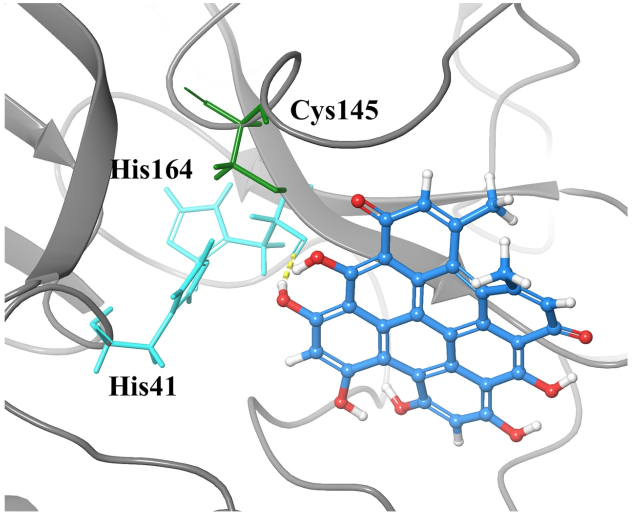

Glide Energy = -51.7 kcal/mol

SRT2104

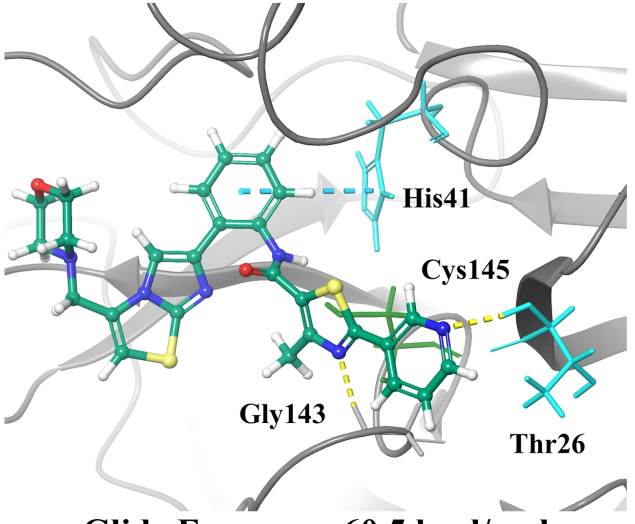

Glide Energy = -60.5 kcal/mol

Cyanidin-3-O-glucoside

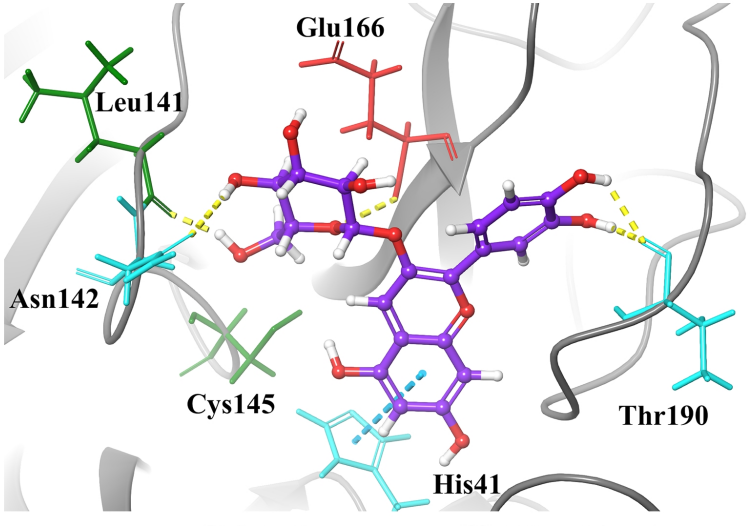

Glide Energy = -62.7 kcal/mol

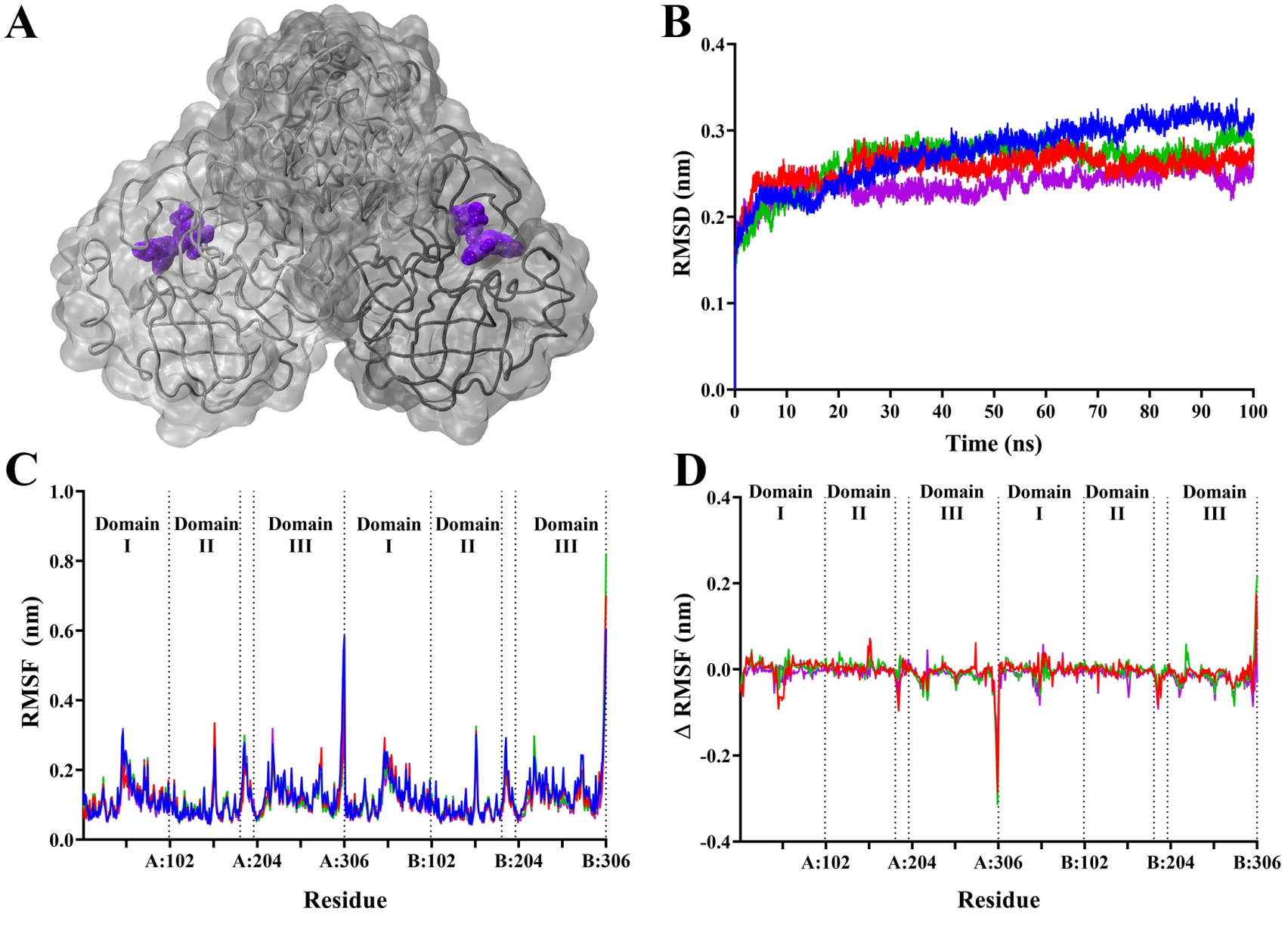
A
B
RMSD (nm)
Time (ns)
C
RMSF (nm)
Domain I
Domain II
Domain III
Domain I
Domain II
Domain III
A:102
A:204
A:306
B:102
B:204
B:306
Residue
D
Δ RMSF (nm)
Domain I
Domain II
Domain III
Domain I
Domain II
Domain III
A:102
A:204
A:306
B:102
B:204
B:306
Residue

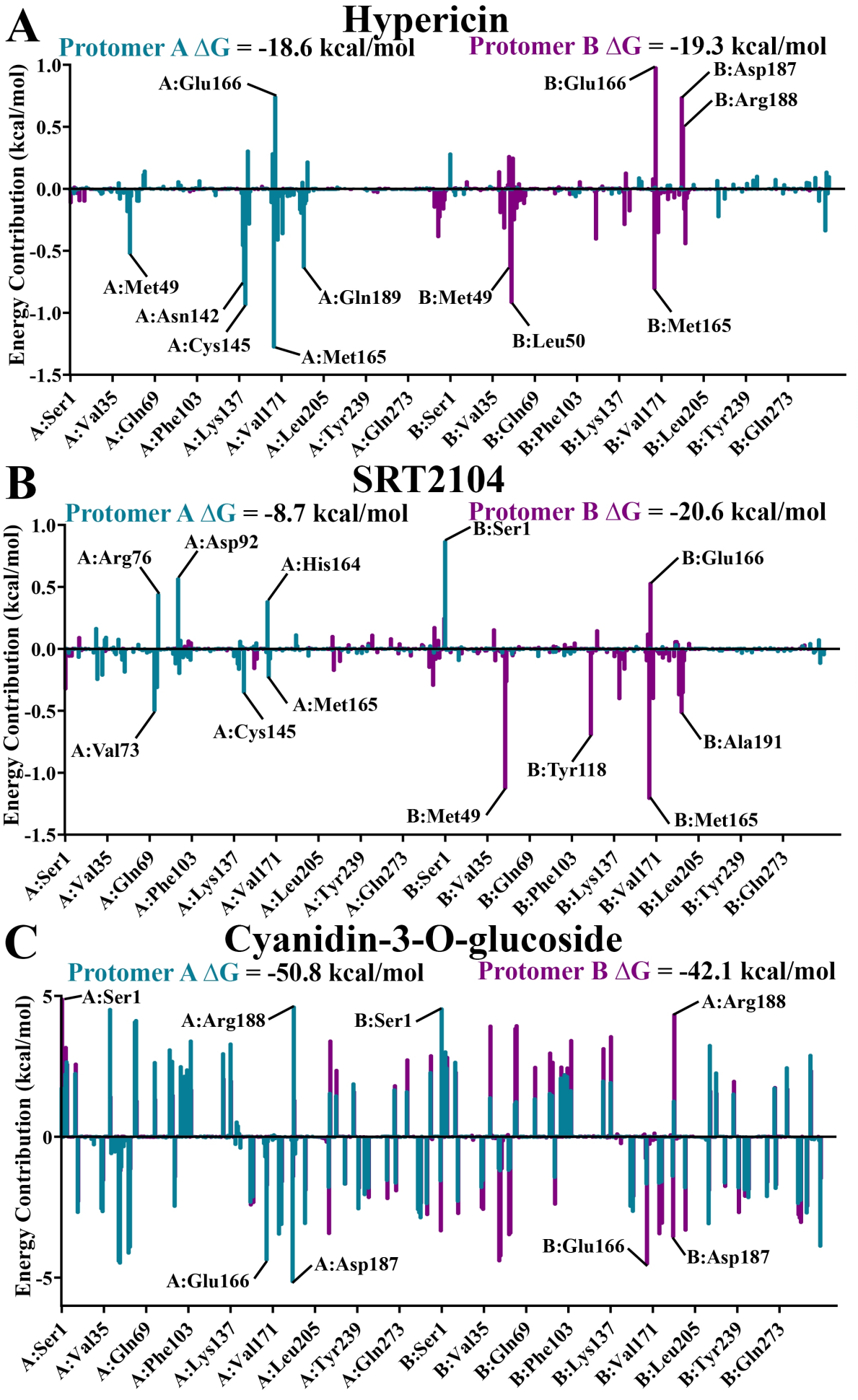
A
Hypericin
Protomer A ΔG = -18.6 kcal/mol
Protomer B ΔG = -19.3 kcal/mol
Energy Contribution (kcal/mol)
1.0
0.5
0.0
-0.5
-1.0
-1.5
A:Glu166
A:Met49
A:Asn142
A:Cys145
A:Gln189
A:Met165
B:Glu166
B:Asp187
B:Arg188
B:Met49
B:Leu50
B:Met165
A:Ser1
A:Val35
A:Gln69
A:Phe103
A:Lys137
A:Val171
A:Leu205
A:Tyr239
A:Gln273
B:Ser1
B:Val35
B:Gln69
B:Phe103
B:Lys137
B:Val171
B:Leu205
B:Tyr239
B:Gln273
B
SRT2104
Protomer A ΔG = -8.7 kcal/mol
Protomer B ΔG = -20.6 kcal/mol
Energy Contribution (kcal/mol)
1.0
0.5
0.0
-0.5
-1.0
-1.5
A:Arg76
A:Asp92
A:His164
A:Met165
A:Cys145
A:Val73
B:Ser1
B:Glu166
B:Ala191
B:Tyr118
B:Met49
B:Met165
A:Ser1
A:Val35
A:Gln69
A:Phe103
A:Lys137
A:Val171
A:Leu205
A:Tyr239
A:Gln273
B:Ser1
B:Val35
B:Gln69
B:Phe103
B:Lys137
B:Val171
B:Leu205
B:Tyr239
B:Gln273
C
Cyanidin-3-O-glucoside
Protomer A ΔG = -50.8 kcal/mol
Protomer B ΔG = -42.1 kcal/mol
Energy Contribution (kcal/mol)
5
0
-5
A:Ser1
A:Arg188
A:Glu166
A:Asp187
B:Ser1
B:Glu166
A:Arg188
B:Asp187
A:Ser1
A:Val35
A:Gln69
A:Phe103
A:Lys137
A:Val171
A:Leu205
A:Tyr239
A:Gln273
B:Ser1
B:Val35
B:Gln69
B:Phe103
B:Lys137
B:Val171
B:Leu205
B:Tyr239
B:Gln273

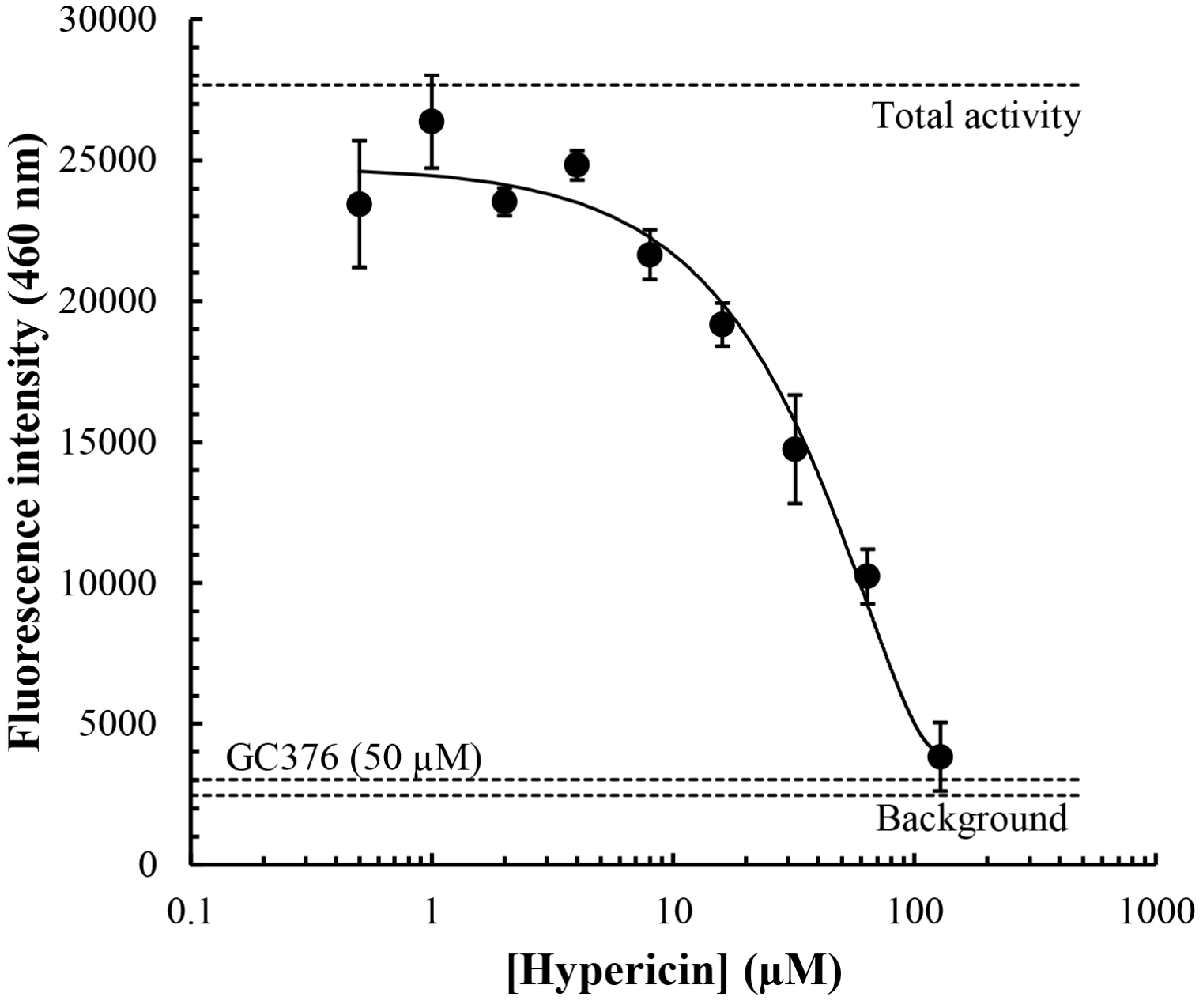
30000
25000
20000
15000
10000
5000
0
Fluorescence intensity (460 nm)
Total activity
GC376 (50 µM)
Background
0.1
1
10
100
1000
[Hypericin] (µM)

Table 1. Binding affinities (kcal/mol) of the compounds that were selected for further investigation.

Compound	**Classification**	**Glide energies (kcal/mol)**
Ritonavir	Protease inhibitor	-71.5
Saquinavir	Protease inhibitor	-77.7
Lopinavir	Protease inhibitor	-56.2
Indinavir	Protease inhibitor	-52.0
Nelfinavir	Protease inhibitor	-65.2
Darunavir	Protease inhibitor	-58.2
Remdesivir	Nucleotide analog	-58.0
Amikacin	Antibiotic	-64.5
Ceftazidime	Antibiotic	-60.5
Baricitinib	Janus kinase inhibitor	-48.8
Suramin	Antiparasitic	-66.3
Hypericin	Anthraquinone derivative	-51.7
SRT2104	Sirtuin activator	-60.5
SRT1720	Sirtuin activator	-60.5
D,L-Sulforaphane glutathione	Isothiocyanate analog	-61.7
(-)-Epicatechin gallate	Natural flavonoid compound	-64.1
Quercitrin	OliveNet™	-60.7
β-Hydroxy verbascoside	OliveNet™	-71.1
β-Hydroxy acteoside	OliveNet™	-67.7
Isoacteoside	OliveNet™	-75.1
Verbascoside	OliveNet™	-76.3
Oxidized verbascoside	OliveNet™	-71.2
Quercetin 3-O-rutinoside	OliveNet™	-77.0
Hesperidin	OliveNet™	-64.0
Rutin	OliveNet™	-69.3
Luteolin-7,4-O-diglucoside	OliveNet™	-66.3
Cyanidin-3-O-glucoside	OliveNet™	-62.7

Table 2: Inhibition of M^{pro} activity by small molecules. Percentage inhibition at a ligand concentration of 50 µM and IC_{50} values calculated using an ELISA

Compound	**IC_{50} (µM) Average ± SEM**	**% Protease inhibition at 50 µM ligand concentration**
Hypericin	63.6 ± 5.7	42.8 ± 8.2
Cyanidin-3-0-glucoside	65.1 ± 14.6	22.6 ± 4.3
SRT2104	85.0 ± 16.8	19.4 ± 6.4
SRT1720	NA*	9.3 ± 2.2
Resveratrol	NA*	1.8 ± 0.9
L-sulforaphane	NA*	8.4 ± 2.7

* Compound concentrations of up to 128µM were used in our experiments; the IC_{50} could not be reached for the ligands noted.

Conflict of interest

Epigenomic Medicine Program (TCK) is supported financially by McCord Research (Iowa, USA), which has a financial interest in dietary compounds described in this work. However, there is no conflict of interest with respect to the inhibition of the SARS-CoV-2 main protease. The remaining co-authors also have no conflicts of interest.

Supplementary Information

Supplementary 1: Selection of 300 Compounds

Table S1: List of the 300 compounds that were used in this *in silico* study. Their binding affinities from Schrödinger (Glide Energy) and AutoDock (Binding Affinity) are provided.

Ligands	Glide Energy (kcal/mol)	Binding Affinity (kcal/mol)	OliveNet™
Jaspolyanoside	-82.0	-8.5	✓
Saquinavir	-77.7	-7.9	
Isojaspolyoside A	-77.5	-8.1	✓
Jaspolyoside	-77.5	-7.8	✓
Quercetin 3-O-rutinoside	-77.0	-9.4	✓
Verbascoside	-76.3	-8.5	✓
Isoacteoside	-75.1	-9.2	✓
Ligstroside derivative 5	-73.4	-7.4	✓
Luteolin-3′,7-O-diglucoside	-71.7	-8.5	✓
Ritonavir	-71.5	-7.6	
Oxidized verbascoside	-71.2	-8.1	✓
β-Hydroxy verbascoside	-71.1	-8.6	✓
Ligstroside derivative 4	-71.0	-7.8	✓
Oleuricine B	-70.6	-5.8	✓
Acteoside	-70.4	-8.6	✓
Orbanchoside	-70.3	-8.3	✓
Scolymoside	-69.7	-7.6	✓
Hellicoside	-69.4	-7.9	✓
Ligstroside derivative 3	-69.3	-7.7	✓
Rutin	-69.3	-7.8	✓
7"-S-Hydroxyoleuropein	-68.9	-7.5	✓
Neo-nüzhenide	-68.8	-7.8	✓
4'-O-β-D-Glucosyl-9-O-(6"-deoxysaccharosyl)olivil	-67.9	-8.1	✓
Suspensaside	-67.7	-8.8	✓
β-Hydroxy-acteoside	-67.7	-8.6	✓
Oleuricine A	-67.3	-7.9	✓
10-Hydroxyoleuropein	-66.7	-7.6	✓
Luteolin-7,4-O-diglucoside	-66.3	-8.3	✓
Oleuropein diglucoside	-66.3	-7.2	✓
Suramin	-66.3	-10.7	
Isoverbascoside	-66.2	-9.1	✓
Apigenin-7-O-rutinoside	-66.1	-8.6	✓
Lucidumoside C	-66.0	-7.8	✓
Nüzhenide 11-Methyl oleoside	-65.3	-8.4	✓
Isorhoifolin	-65.3	-8.6	✓
Nelfinavir	-65.2	-8.3	

Oleuropein-3'-O-β-D-glucopyranoside	-64.6	-7.3	✓
Amikacin	-64.5	-6.1	
(-)-Epicatechin gallate	-64.1	-8.2	
Hesperidin	-64.0	-8.8	✓
Oleuropein-3"-Methyl ether	-63.6	-7.8	✓
Cyanidin-3-O-glucoside	-62.7	-8.7	✓
Demethyloleuropein	-62.5	-8.2	✓
Demethyloleuropein (l-shaped)	-62.5	-7.9	✓
Oxidized isoverbascoside	-62.4	-9.1	✓
Oleuroside-10-carboxylic acid	-61.9	-7.9	✓
Nüzhenide	-61.8	-8.8	✓
D,L-Sulforaphane glutathione	-61.7	-6.3	
Luteolin-8-C-glucoside	-61.2	-8.8	✓
Quercitrin	-60.7	-8.9	✓
Quercetin-3-O-glucoside	-60.6	-8.2	✓
Dihydro-oleuropein	-60.5	-7.1	✓
Ceftazidime	-60.5	-7.7	
SRT2104	-60.5	-8.6	
SRT1720	-60.5	-9.1	
Quercetin-3-rhamnoside	-60.1	-8.8	✓
Nüzhenide oleoside	-60.1	-8.1	✓
Cyanidin-3-O-rutinoside	-60.0	-8.8	✓
Oleuropein	-59.6	-8.0	✓
Oleuroside	-59.1	-7.6	✓
Quercetin-7-O-glucoside	-58.4	-8.6	✓
Delphinidin-3-O-glucoside	-58.3	-8.3	✓
Darunavir	-58.2	-7.1	
Luteolin-6-C-glucoside	-58.1	-7.8	✓
Ligstroside	-58.1	-7.9	✓
Remdesivir	-58.0	-7.5	
10-Hydroxy oleuropein aglycone	-56.7	-7.2	✓
Ligstroside-3'-O-β-D-glucopyranoside	-56.6	-7.4	✓
Luteolin-4'-O-rutinoside	-56.5	-8.9	✓
Wedelosin	-56.2	-7.2	✓
Lopinavir	-56.2	-8.0	
Ligstroside derivative 2	-56.2	-6.9	✓
Hydroxytyrosol diglucoside	-56.0	-8.2	✓
Ceftriaxone	-55.9	-8.1	
Luteolin-7-O-glucoside	-55.7	-8.3	✓
Ligstroside derivative 1	-55.3	-7.5	✓
Luteolin-4’-O-glucoside	-55.0	-7.6	✓
Luteolin-7-O-rutinoside	-54.9	-8.3	✓
Elenolic acid diglucoside	-54.9	-7.4	✓
Vicenin-2	-54.8	-8.4	✓
Demethylligstroside	-54.1	-7.4	✓
Apigenin-7-O-glucoside	-53.8	-8.0	✓

Oleuropeindial - Lactone (Cannizzaro-like product of oleuropeindial)	-53.3	-7.3	✓
Caffeoyl-6'-secologanoside	-53.1	-7.8	✓
6'-β-D-Glucopyranosyl oleoside	-53.0	-8.3	✓
(+)-Fraxiresinol-1-β-D-glucopyranoside	-52.6	-7.9	✓
(+)-1-Acetoxypinoresinol-4'-β-D-glucopyranoside-4"-O-methyl ether	-52.0	-7.3	✓
(+)-1-Hydroxypinoresinol-4"-O-methyl ether	-52.0	-7.3	✓
Hydroxytyrosil elenolate	-52.0	-7.2	✓
Indinavir	-52.0	-8.2	
Hypericin	-51.7	-10.2	
Cefotaxime	-51.4	-7.2	
Comselogoside	-51.1	-8.1	✓
Tobramycin	-51.1	-5.9	
3-Acetyloxy berchemol	-50.9	-6.7	✓
Esculin	-50.6	-7.4	✓
Chrysoeriol-7-O-glucoside	-50.4	-8.1	✓
6'-Rhamnopyranosyl oleoside	-50.3	-7.7	✓
Curcumin	-50.3	-7.4	
10-Hydroxy-10-methyl oleuropein aglycone	-50.1	-6.8	✓
Demethoxycurcumin	-49.8	-7.5	
Oleuropeindial (keto form)	-49.6	-6.6	✓
Hemiacetal of dialdehydic oleuropein aglycone decarboxymethyl	-49.3	-6.8	✓
1-Acetoxypinoresinol	-49.2	-6.7	✓
Ertapenem	-48.9	-7.6	
Baricitinib	-48.8	-8.2	
(+)-1-Hydroxypinoresinol-4'-β-D-glucopyranoside	-48.8	-7.5	✓
Demethyloleuropein aglycone (enol form)	-48.8	-7.4	✓
Methoxyluteolin	-48.7	-7.6	✓
Hydroxytyrosol acyclodihydroelenolate	-48.4	-6.7	✓
Ligstroside aglycone	-48.4	-6.8	✓
Oleuropeindial (Cannizzaro-like product of oleuropeindial)	-48.3	-7.3	✓
Monoaldehydic form of Oleuropein aglycon	-48.1	-7.3	✓
Cefuroxime	-47.9	-6.6	
3,4-DHPEA-EDA (Oleuropein-aglycone di-aldehyde)	-47.8	-6.7	✓
Syringaresinol	-47.7	-7.4	✓
Baicalin	-47.6	-8.5	
Berchemol	-47.6	-7.4	✓

3,4-DHPEA-DETA	-47.6	-7.1	✓
Loganin	-47.3	-6.9	✓
Rosmarinic acid	-47.3	-7.8	✓
Delphinidin	-47.3	-7.4	✓
Hydroxytyrosil-elenolate	-47.1	-6.8	✓
Monoaldehydic form of Ligstroside aglycon	-46.9	-6.9	✓
Nafamostat	-46.7	-7.7	
3,4-DHPEA-DEDA (acetal)	-46.7	-6.3	✓
Oleacein (Dialdehydic form of decarboxymethyl Oleuropein aglycon)	-46.5	-6.8	✓
10-Hydroxy oleuropein aglycone decarboxymethyl	-46.4	-6.8	✓
Caffeoylglucose	-46.3	-8.0	✓
Oleoside dimethylester	-46.0	-6.5	✓
Ligstroside aglycone methyl acetal	-45.9	-7.4	✓
D,L-Sulforaphane N-acetyl-L-cysteine	-45.6	-5.8	
Hydroxytyrosol-1′-β-glucoside	-45.3	-7.2	✓
Sulfasalazine	-45.2	-8.0	
Hydroxytyrosol-4-β-glucoside	-45.0	-6.8	✓
Oleuropein aglycone (3,4-DHPEA-EA)	-44.9	-6.9	✓
Oleoside-11-Methylester	-44.9	-7.3	✓
Eriodictyol	-44.7	-7.5	✓
Secologanoside	-44.7	-6.5	✓
Oleohydroxypyterol	-44.6	-6.3	✓
Amoxicillin	-44.3	-7.8	
7-Deoxyloganic acid	-44.2	-7.3	✓
Azithromycin	-44.0	-5.5	
Doripenem	-44.0	-7.4	
Catechin	-43.8	-7.2	
Arbidol	-43.8	-6.3	
(+)-1-Acetoxypinoresinol-4'-β-D-glucopyranoside	-43.7	-7.4	✓
Demethyloleuropein aglycone	-43.7	-7.4	✓
Quercetin	-43.6	-7.5	✓
Luteolin	-43.6	-7.4	✓
(+)-Cycloolivil	-43.5	-6.7	✓
Cornoside	-43.4	-7.1	✓
Hemiacetal of dialdehydic ligstroside aglycone decarboxymethyl	-43.3	-6.2	✓
Fangicholine	-43.3	-7.4	
Secologanin	-43.3	-6.4	✓
Scopolin	-43.1	-7.7	✓
Hydroxytyrosol-3-β-glucoside	-43.0	-6.2	✓
1-oleyltyrosol	-42.8	-5.9	✓
Decarboxymethyl ligstroside aglycone	-42.6	-7.3	✓

Hesperitin	-42.5	-7.3	✓
(+)-1-Acetoxypinoresinol-4"-O-methyl ether	-42.4	-6.8	✓
Indomethacin	-42.3	-7.6	
Chrysoeriol	-42.2	-7.3	✓
D,L-Sulforaphane-L-cysteine	-42.2	-5.2	
Cepharanthine	-41.9	-8.0	
Elenolic acid glucoside	-41.9	-6.9	✓
Oleocanthal (Dialdehydic form of decarboxymethyl Ligstroside aglycon)	-41.8	-6.5	✓
Chlorogenic acid	-41.7	-7.6	✓
Naringenin	-41.5	-7.7	
Demethyloleuropein aglycone dialdehyde	-41.4	-7.1	✓
Kaempferol	-41.3	-7.7	
Loganic acid	-41.2	-7.1	✓
Levofloxacin	-41.1	-7.3	
Diosmetin	-41.0	-7.4	✓
Hydroxytyrosol rhamnoside	-41.0	-7.0	✓
Imipenem	-40.9	-6.2	
Secologanol	-40.9	-6.2	✓
Pinoresinol	-40.7	-7.8	✓
Secologanic acid	-40.7	-7.6	✓
Cyanidin (cation)	-40.4	-7.3	✓
p-HPEA-EDA	-40.0	-6.2	✓
Moxifloxacin	-39.9	-7.8	
Disulfiram	-39.7	-4.4	
Ergosterol	-39.5	-7.4	
Tetrandine	-39.3	-7.2	
Chloroquine	-39.3	-5.8	
Apigenin	-39.3	-7.7	✓
Ciprofloxacin	-39.1	-7.7	
Ampicillin	-39.1	-6.7	
Gingerol	-39.0	-5.8	
Caftaric acid	-38.3	-7.3	✓
Deoxyloganic acid lauryl ester	-38.3	-5.6	✓
Pterostilbene	-38.2	-6.5	
Salidroside	-38.2	-7.0	✓
Taxifolin	-38.2	-7.4	✓
Verucosin	-38.2	-7.3	✓
1-(3'-Methoxy-4'-hydroxy)- phenyl-6,7-dihydroxyisochroman	-37.6	-7.0	✓
Chloroquine Phosphate	-37.5	-5.7	
Meropenem	-37.4	-7.0	
Hydroxychloroquine	-37.0	-6.5	
Dihydrotanshinone	-36.8	-7.8	
Oleoside	-36.5	-6.8	✓

Linoleic acid	-36.4	-5.1	✓
Oseltamivir	-36.4	-6.2	
Elaidic acid	-35.7	-4.6	✓
Penicillin	-35.5	-7.3	
Melatonin	-35.4	-6.2	
Petroselinic acid	-35.3	-4.9	✓
Emodin	-34.8	-7.3	
Quinine	-34.7	-7.0	
Elenolic acid methylester	-34.2	-5.6	✓
Oleic acid	-34.0	-4.9	✓
Linoelaidic acid	-33.9	-5.2	✓
D-(+)-Erythro-1-(4-hydroxy-3-methoxy)- 214 - phenyl-1,2,3-propantriol	-33.4	-5.9	✓
Shionone	-33.0	-7.7	
Hydroxytyrosol acetate	-32.8	-5.9	✓
Tyrosol acetate	-32.7	-5.7	✓
1-Phenyl-6,7-dihydroxyisochroman	-32.7	-6.7	✓
Cis-10-Heptadecenoic Acid	-32.3	-4.9	✓
Resveratrol	-32.0	-6.9	
Trans-palmiteolieic acid	-31.7	-4.8	✓
Esculetin	-31.7	-6.2	✓
Sulforaphane	-31.5	-3.9	
Sulfamethoxazole	-31.2	-6.7	
Zingerol	-30.8	-5.5	
Palmitic acid	-30.7	-4.5	✓
Vaccenic acid	-30.1	-5.1	✓
Scopoletin	-29.8	-5.8	✓
Myristic acid	-29.3	-4.7	✓
Trimethoprim	-29.2	-6.4	
DEDA acetal	-28.7	-5.0	✓
2,3-dihydrocaffeic acid	-28.7	-5.4	✓
Margaric acid	-28.5	-4.8	✓
Homovanillyl alcohol	-28.2	-5.1	✓
Elenolic acid	-28.2	-5.7	✓
3,4-Dihydroxyphenylglycol	-28.1	-5.5	✓
Acetaminophen	-28.1	-5.2	
Dialdehydic elenolic ester decarboxymethyl	-27.9	-4.8	✓
3,4,5-Trimethoxybenzoic acid	-27.7	-5.5	✓
Palmitoleic acid	-27.3	-5.0	✓
2,5-Dihydroxyphenylacetic acid	-26.9	-5.3	✓
Clavulanic acid	-26.3	-6.0	
Hydroxytyrosol	-26.3	-5.2	✓
Demethyl elenolic acid	-26.2	-5.8	✓
Ferulic acid	-26.1	-5.6	✓
Homovanillin	-26.0	-5.0	✓

Lauric acid	-25.9	-4.7	✓
Syringaldehyde	-25.7	-5.2	✓
Syringic acid	-25.5	-5.5	✓
Sinapic acid	-25.4	-5.8	✓
Dialdehydic elenolic acid decarboxymethyl	-25.4	-4.7	✓
Aspirin	-25.4	-5.1	
Hydroxycaffeic acid	-25.4	-5.9	✓
m-Coumaric acid	-25.3	-5.4	✓
o-Coumaric acid	-24.5	-5.2	✓
Tyrosol	-24.2	-4.6	✓
Isoeugenol	-24.2	-5.2	✓
Caffeic acid	-24.2	-7.9	✓
4-Hydroxy-3-methoxy-phenylacetic acid	-24.0	-5.4	✓
4-O-methyl-D-glucuronic acid	-24.0	-5.4	✓
Quinic acid	-23.9	-5.4	✓
4-Ethylguaiacol	-23.8	-4.8	✓
Gallic acid	-23.6	-5.5	✓
Dihydro-p-coumaric acid	-23.5	-5.1	✓
4-Hydroxybenzaldehyde	-23.4	-4.6	✓
3,4-Dihydroxyphenylacetic acid	-23.4	-5.6	✓
Phloretic acid	-23.1	-5.2	✓
Gentisic acid	-23.0	-5.2	✓
Shikimic acid	-23.0	-5.3	✓
2,4 dihydroxybenzoic acid	-23.0	-5.3	✓
p-cresol	-23.0	-4.2	✓
DEDA (Decarboxymethyl elenolic acid dialdehyde)	-22.9	-4.8	✓
4-Vinylguaiacol	-22.8	-4.9	✓
Acetylcysteine	-22.7	-4.6	
Protocatechuic acid	-22.6	-5.3	✓
4-Vinylphenol	-21.9	-4.4	✓
Fructosamine	-21.9	-5.0	
Homovanillic acid	-21.8	-5.2	✓
Guaiacol	-21.5	-4.5	✓
Allicin	-20.9	-3.7	
3,4-Dimethoxybenzoic acid	-20.7	-5.4	✓
2-Methoxy-4-vinylphenol	-20.7	-4.9	✓
p-Coumaric acid	-20.7	-5.2	✓
Vanillic acid	-20.7	-5.3	✓
Cinnamic acid	-20.6	-5.0	✓
m-cresol	-20.3	-4.4	✓
4-Methylcatechol	-20.2	-5.0	✓
Homoveratric acid	-20.2	-5.5	✓
Menthol	-20.0	-4.7	
4-Ethylphenol	-19.8	-4.4	✓

2,6-Dihydroxybenzoic acid	-19.7	-5.1	✓
Catechol	-18.5	-4.6	✓
o-cresol	-18.3	-4.0	✓
Patchouli alcohol	-17.6	-5.1	
Phenol	-16.8	-3.9	✓
Metformin	-16.7	-4.7	
4-hydroxybenzoic acid	-16.3	-4.8	✓
Simeprevir		-8.5	
Ivermectin		-7.6	
Ebselen		-6.5	
α-ketoamide 13b inhibitor	-65.7	-7.7	

Supplementary 2: Selection of 30 compounds

Table S2: The structures of the 27 compounds that were predicted by the Schrödinger program to bind to the active site of the M^{pro} monomer and were selected to undergo blind docking on the M^{pro} dimer are provided.

Compound	Classification	Glide Energies: kcal/mol	Structures
Ritonavir	Protease inhibitor	-71.5	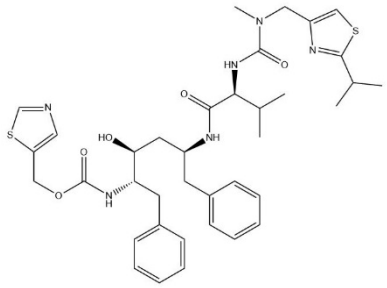
Saquinavir	Protease inhibitor	-77.7	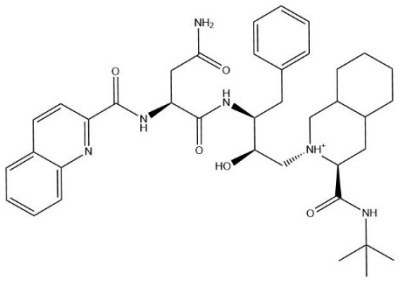
Lopinavir	Protease inhibitor	-56.2	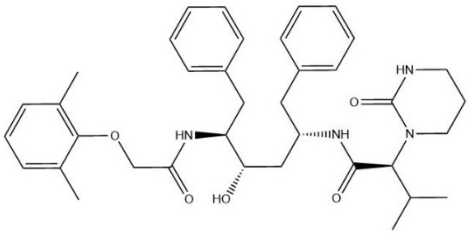
Indinavir	Protease inhibitor	-52.0	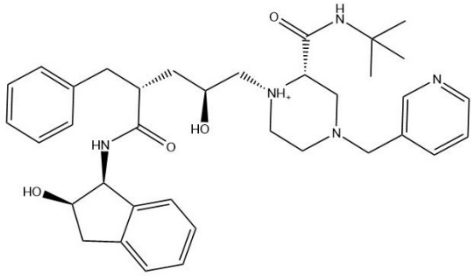

Nelfinavir	Protease inhibitor	-65.2	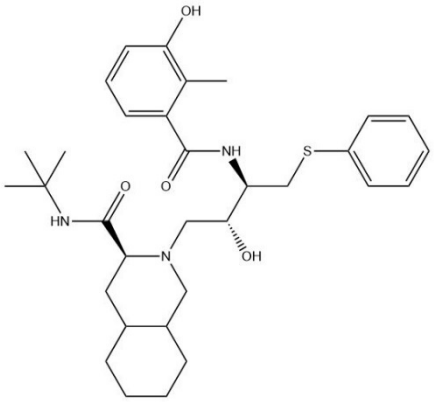
Darunavir	Protease inhibitor	-58.2	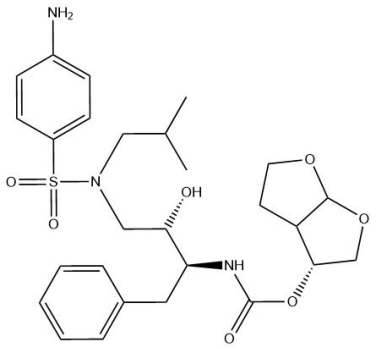
Remdesivir	Nucleotide analog	-58.0	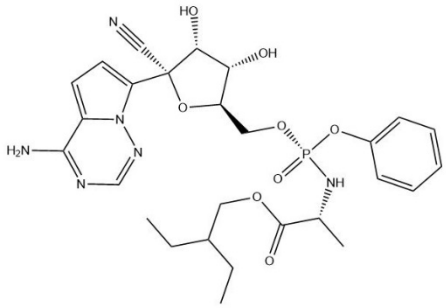
Amikacin	Antibiotic	-64.5	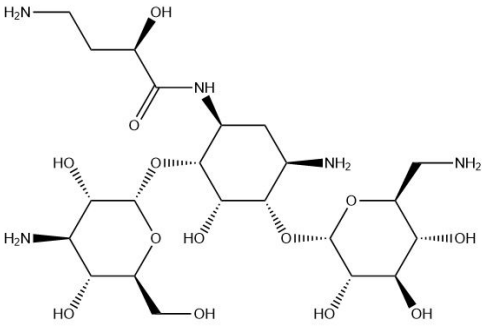

Ceftazidime	Antibiotic	-60.5	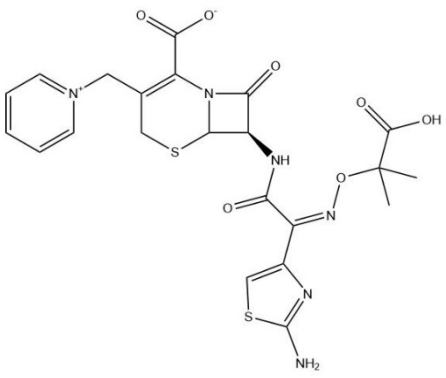
Baricitinib	Janus kinase inhibitor	-48.8	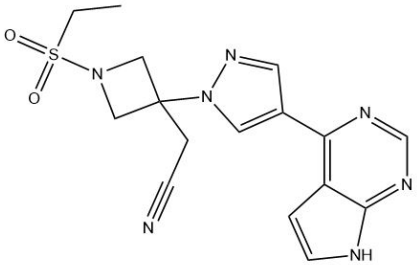
Suramin	Antiparasitic	-66.3	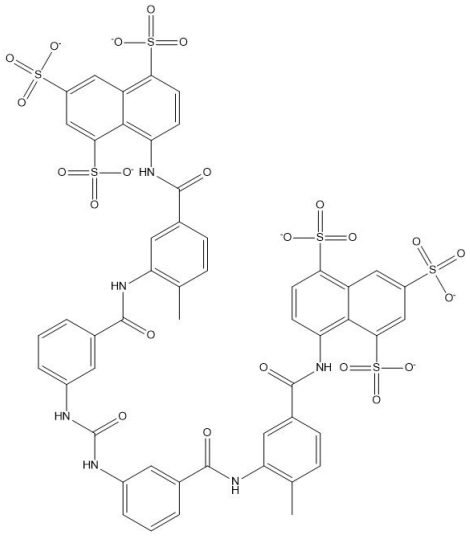
Hypericin	Anthraquinone derivative	-51.7	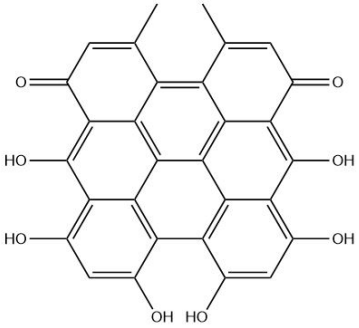

SRT2104	Sirtuin activator	-60.5	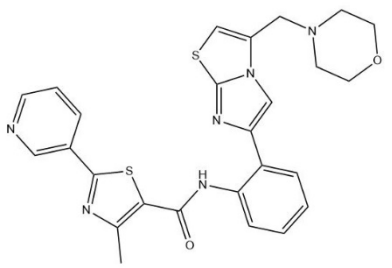
SRT1720	Sirtuin activator	-60.5	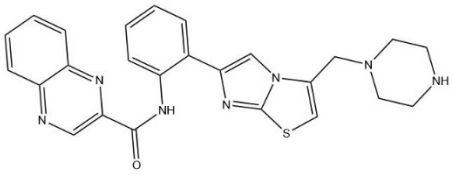
D,L-Sulforaphane glutathione	Isothiocyanate analog	-61.7	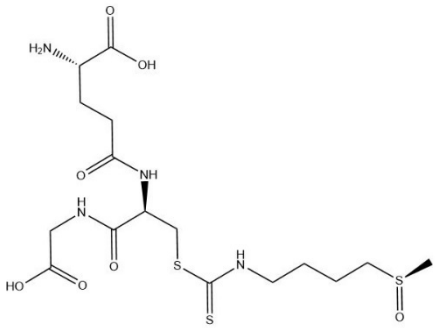
(-)-Epicatechin gallate	Natural flavonoid compound	-64.1	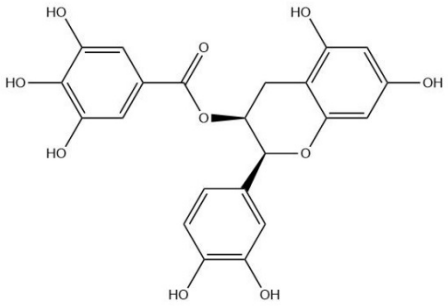
Quercitrin	OliveNet™	-60.7	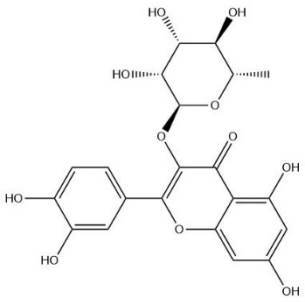

β-Hydroxy verbascoside	OliveNet™	-71.1	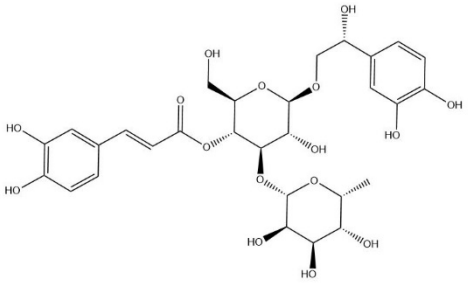
β-Hydroxy acteoside	OliveNet™	-67.7	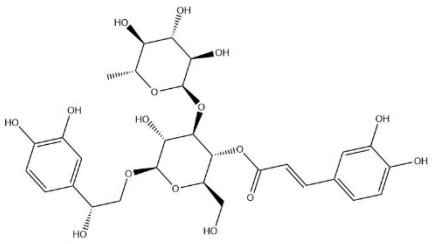
Isoacteoside	OliveNet™	-75.1	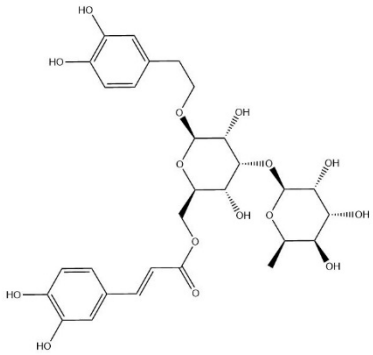
Verbascoside	OliveNet™	-76.3	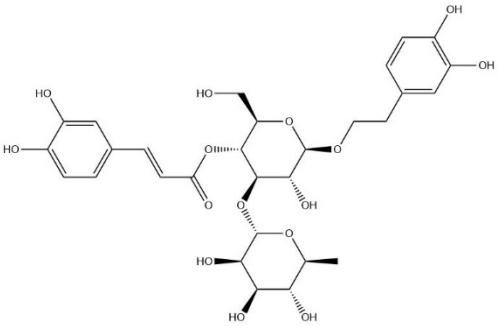
Oxidized verbascoside	OliveNet™	-71.2	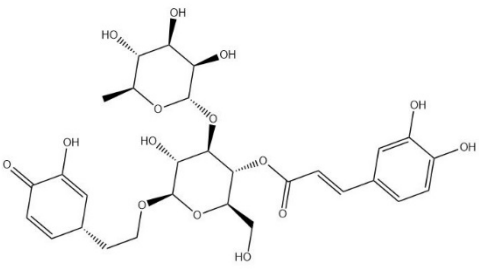

Quercetin 3-O-rutinoside	OliveNet™	-77.0	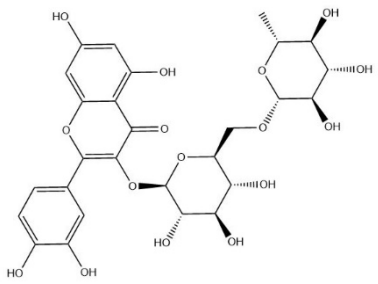
Hesperidin	OliveNet™	-64.0	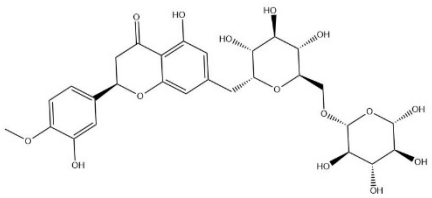
Rutin	OliveNet™	-69.3	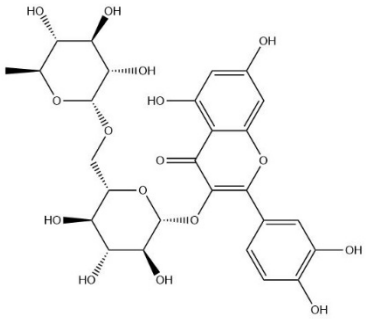
Luteolin-7,4-O-diglucoside	OliveNet™	-66.3	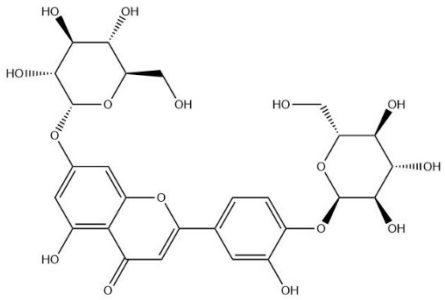

Cyanidin-3-O-glucoside	OliveNet^{TM}	-62.7	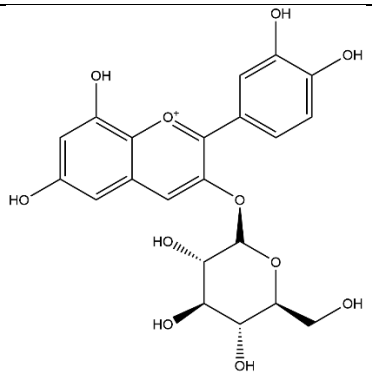

Supplementary 3: Blind docking results for hypericin, cyanidin-3-O-glucoside and SRT2104

Table S3: The blind docking results from AutoDock Vina are provided for the α-ketoamide inhibitor.

Compound:	**α-ketoamide inhibitor**			
	MONOMER		**DIMER**	
Pose Ranking	**Pose affinity (kcal/mol)**	**Site of binding**	**Pose affinity (kcal/mol)**	**Site of binding**
1	-7.7	Active	-9.4	Allosteric
2	-7.7	Active	-9.4	Allosteric
3	-7.6	Active	-9.1	Allosteric
4	-7.6	Active	-9.1	Allosteric
5	-7.5	Active	-9.1	Allosteric
6	-7.4	Active	-9.1	Allosteric
7	-7.4	Active	-9.1	Allosteric
8	-7.4	Active	-9.1	Allosteric
9	-7.4	Active	-9.1	Allosteric
10	-7.3	Active	-8.9	Allosteric
11	-7.3	Active	-8.9	Allosteric
12	-7.3	Active	-8.9	Allosteric
13	-7.3	Active	-8.8	Allosteric
14	-7.3	Active	-8.8	Allosteric
15	-7.2	Allosteric	-8.8	Allosteric
16	-7.2	Active	-8.7	Active
17	-7.2	Active	-8.7	Allosteric
18	-7.2	Active	-8.7	Allosteric
19	-7.1	Allosteric	-8.7	Allosteric
20	-7.1	Active	-8.6	Allosteric
	Total poses in active site =	**18**	**Total poses in active site =**	**1**

Table S4: The blind docking results from AutoDock Vina are provided for hypericin.

Compound:	**Hypericin**			
	MONOMER		**DIMER**	
Pose Ranking	**Pose affinity (kcal/mol)**	**Site of binding**	**Pose affinity (kcal/mol)**	**Site of binding**
1	-9.4	Active	-10.2	Active
2	-9.4	Active	-10.2	Active
3	-8.6	Allosteric	-10.2	Active
4	-8.6	Allosteric	-10.2	Active
5	-8.5	Allosteric	-10.0	Allosteric
6	-8.5	Allosteric	-9.9	Allosteric
7	-8.4	Active	-9.9	Allosteric
8	-8.4	Active	-9.9	Allosteric
9	-8.4	Allosteric	-9.8	Allosteric
10	-8.4	Allosteric	-9.8	Allosteric
11	-8.4	Allosteric	-9.8	Allosteric
12	-8.3	Allosteric	-9.8	Allosteric
13	-8.3	Allosteric	-9.7	Allosteric
14	-8.3	Allosteric	-9.7	Allosteric
15	-8.3	Allosteric	-9.7	Allosteric
16	-8.3	Allosteric	-9.7	Allosteric
17	-8.2	Allosteric	-9.7	Allosteric
18	-8.1	Allosteric	-9.7	Allosteric
19	-8.0	Active	-9.7	Allosteric
20	-8.0	Active	-9.7	Allosteric
	Total poses in active site =	**6**	**Total poses in active site =**	**4**

Table S5: The blind docking results from AutoDock Vina are provided for cyanidin-3-O-glucoside.

Compound:	**Cyanidin-3-O-glucoside**			
	MONOMER		**DIMER**	
Pose Ranking	**Pose affinity (kcal/mol)**	**Site of binding**	**Pose affinity (kcal/mol)**	**Site of binding**
1	-8.7	Active	-8.8	Active
2	-8.7	Active	-8.8	Active
3	-8.6	Active	-8.6	Active
4	-8.0	Active	-8.6	Active
5	-7.9	Active	-8.5	Allosteric
6	-7.9	Active	-8.5	Allosteric
7	-7.9	Active	-8.4	Allosteric
8	-7.8	Active	-8.4	Allosteric
9	-7.8	Active	-8.4	Allosteric
10	-7.8	Active	-8.4	Allosteric
11	-7.7	Active	-8.2	Active
12	-7.7	Active	-8.2	Active
13	-7.6	Allosteric	-8.2	Allosteric
14	-7.5	Active	-8.2	Allosteric
15	-7.5	Active	-8.1	Active
16	-7.5	Active	-8.1	Allosteric
17	-7.5	Active	-8.1	Allosteric
18	-7.3	Active	-8.1	Allosteric
19	-7.6	Active	-8.0	Allosteric
20	-7.2	Active	-8.0	Allosteric
	Total poses in active site =	**19**	**Total poses in active site =**	**7**

Table S6: The blind docking results from AutoDock Vina are provided for SRT2104.

Compound:	**SRT2104**			
	MONOMER		**DIMER**	
Pose Ranking	**Pose affinity (kcal/mol)**	**Site of binding**	**Pose affinity (kcal/mol)**	**Site of binding**
1	-8.7	Active	-9.2	Active
2	-8.4	Active	-9.2	Allosteric
3	-8.4	Active	-9.2	Active
4	-8.4	Active	-9.2	Allosteric
5	-8.4	Active	-9.1	Allosteric
6	-8.4	Active	-9.1	Allosteric
7	-8.2	Active	-9.1	Allosteric
8	-8.2	Active	-9.1	Allosteric
9	-8.1	Active	-8.9	Allosteric
10	-8.1	Active	-8.8	Active
11	-8.0	Active	-8.8	Active
12	-8.0	Active	-8.8	Allosteric
13	-8.0	Active	-8.7	Allosteric
14	-7.9	Active	-8.7	Allosteric
15	-7.9	Allosteric	-8.7	Allosteric
16	-7.9	Active	-8.7	Allosteric
17	-7.9	Active	-8.6	Allosteric
18	-7.9	Allosteric	-8.6	Allosteric
19	-7.8	Active	-8.6	Allosteric
20	-7.8	Active	-8.6	Allosteric
	Total poses in active site =	**18**	**Total poses in active site =**	**4**

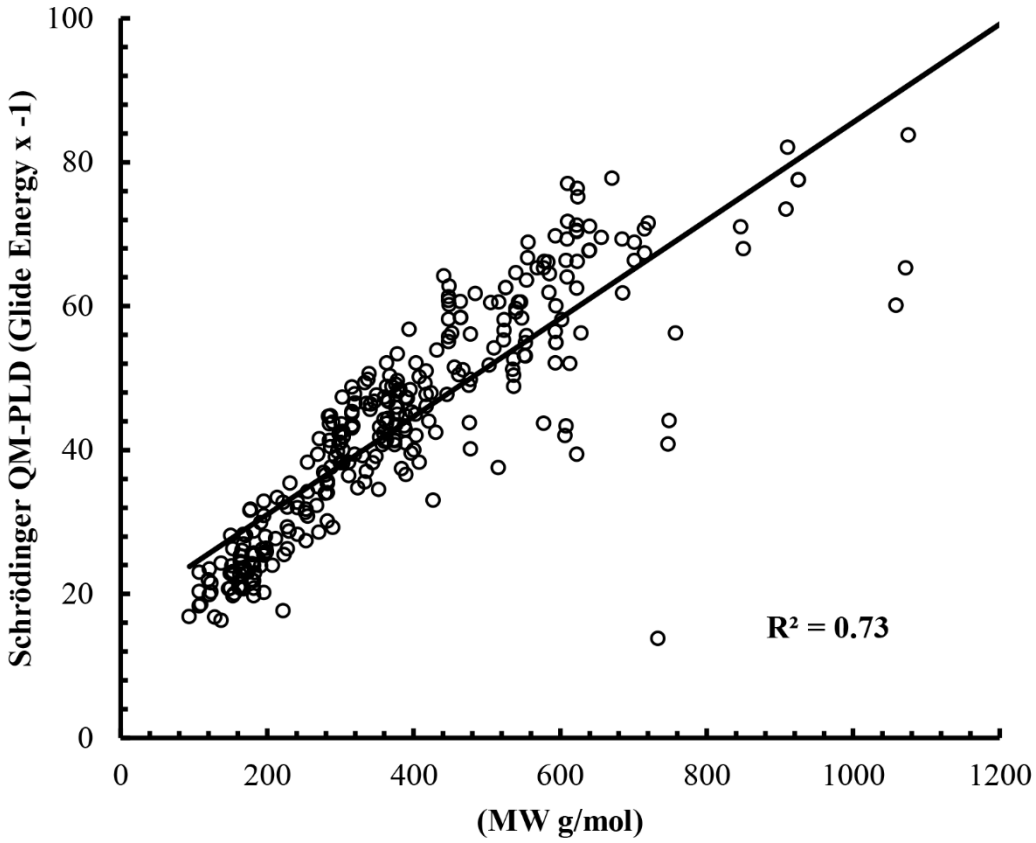

Figure S1: Correlation of Schrödinger QM-PLD Glide Energy scores with the molecular weight of the 300 compounds that were used in the initial screen.

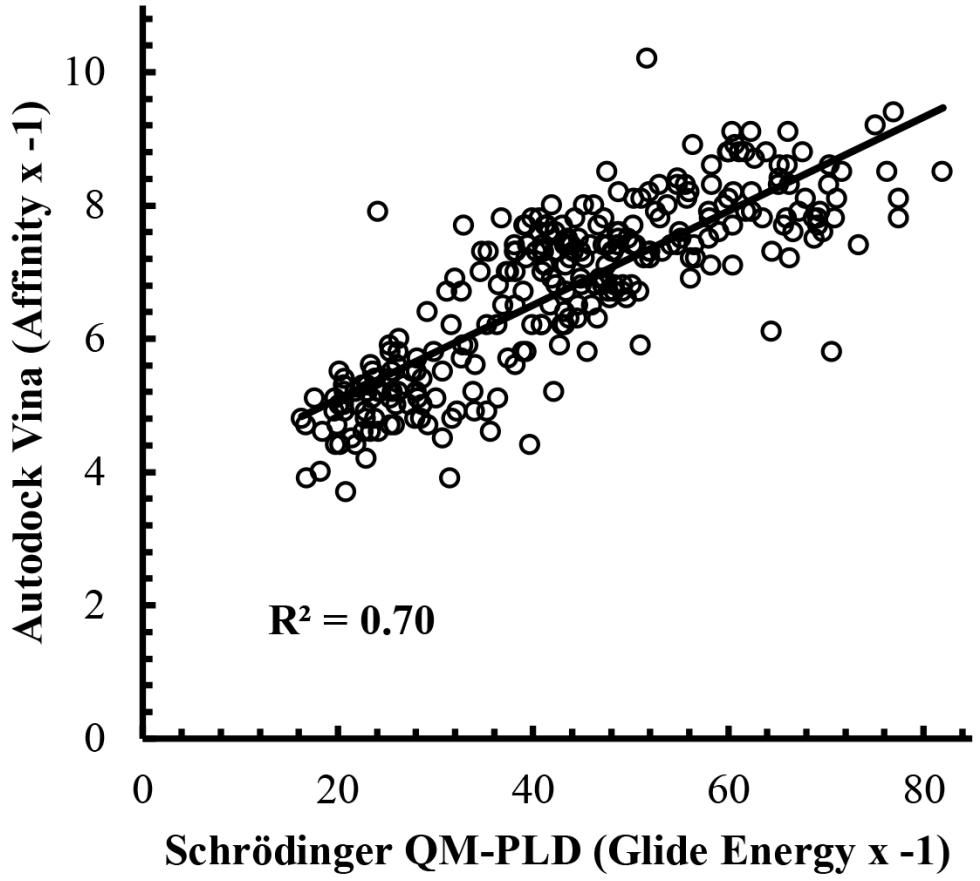

Figure S2: Correlation between Schrödinger QM-PLD Glide Energy scores and binding affinity scores from Autodock Vina for the 300 compounds that were used in the initial screen.

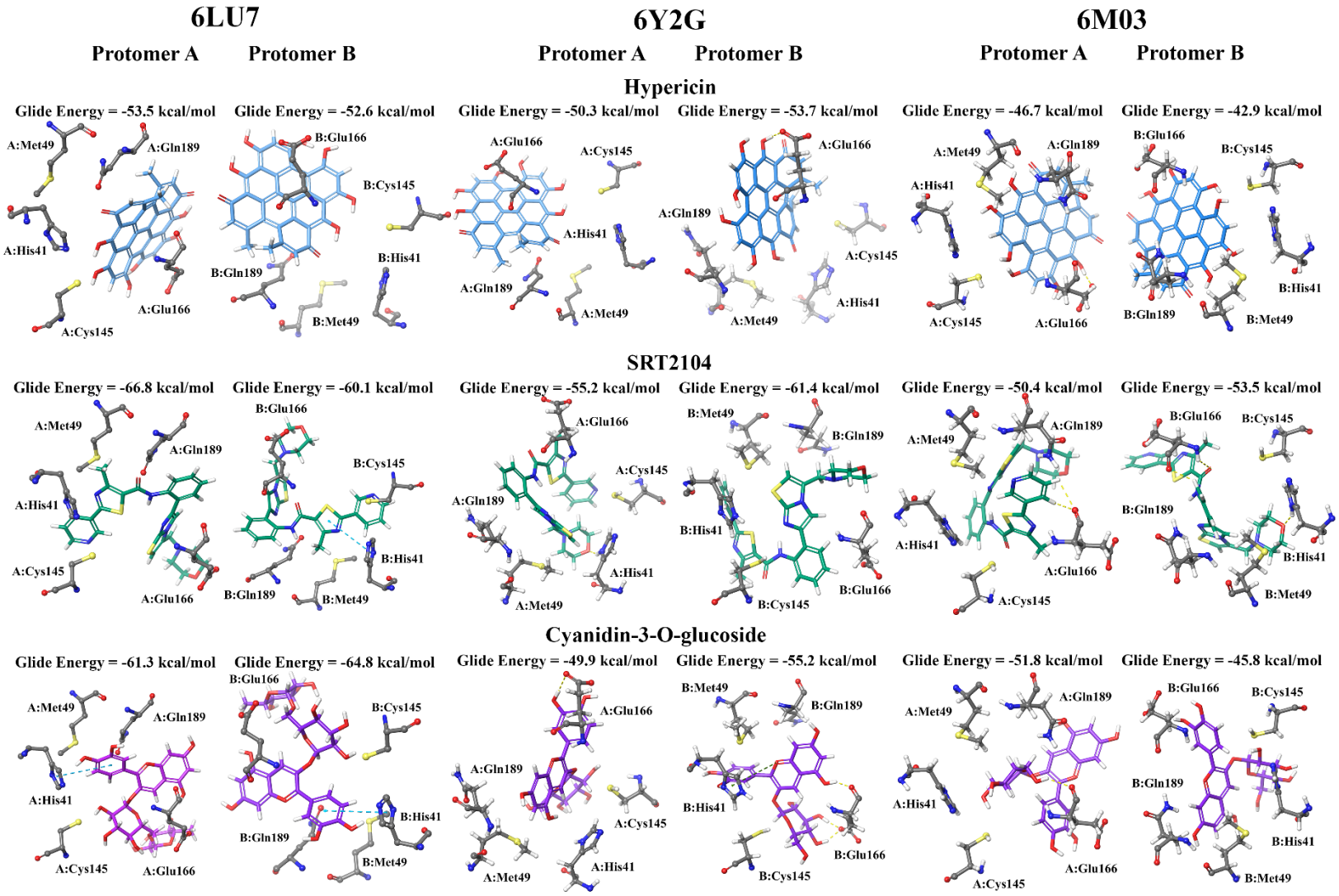

Figure S3: Comparison between docking to the active site of SARS-CoV-2 M^{pro} structures (PDB ID: 6LU7, 6Y2G, and 6M03) in protomers A and B. Hydrogen bonds are shown as yellow, pi-pi stacking in blue, and pi-cation bonds in green dashed lines.

Movie S1. 100 ns trajectory of the apo form of the SARS-CoV-2 main protease

Movie S2. 100 ns trajectory of hypericin bound to the active site of the SARS-CoV-2 main protease

Movie S3. 100 ns trajectory of SRT2104 bound to the active site of the SARS-CoV-2 main protease

Movie S4. 100 ns trajectory of cyanidin-3-O-glucoside bound to the active site of the SARS-CoV-2 main protease